SANDIA REPORT
SAND20XX-XXXX
Printed Click to enter a date

Sandia National Laboratories

Single Photon Detection with On-Chip Number Resolving Capability

Eric Chatterjee, Org. 8648
Paul Davids, Org. 5265
Tina Nenoff, Org. 1800
Wei Pan, Org. 8342
David Rademacher, Org. 1874
Daniel Soh, Org. 8648

Prepared by
Sandia National Laboratories
Albuquerque, New Mexico
87185 and Livermore,
California 94550

Issued by Sandia National Laboratories, operated for the United States Department of Energy by National Technology & Engineering Solutions of Sandia, LLC.

Available to DOE and DOE contractors from
U.S. Department of Energy
Office of Scientific and Technical Information
P.O. Box 62
Oak Ridge, TN 37831

Telephone: (865) 576-8401
Facsimile: (865) 576-5728
E-Mail: reports@osti.gov
Online ordering: http://www.osti.gov/scitech

Available to the public from
U.S. Department of Commerce
National Technical Information Service
5301 Shawnee Rd
Alexandria, VA 22312

Telephone: (800) 553-6847
Facsimile: (703) 605-6900
E-Mail: orders@ntis.gov
Online order: https://classic.ntis.gov/help/order-methods/

ABSTRACT

Single photon detection (SPD) plays an important role in many forefront areas of fundamental science and advanced engineering applications. In recent years, rapid developments in superconducting quantum computation, quantum key distribution, and quantum sensing call for SPD in the microwave frequency range. We have explored in this LDRD project a new approach to SPD in an effort to provide deterministic photon-number-resolving capability by using topological Josephson junction structures. In this SAND report, we will present results from our experimental studies of microwave response and theoretical simulations of microwave photon number resolving detector in topological Dirac semimetal Cd_3As_2. These results are promising for SPD at the microwave frequencies using topological quantum materials.

ACKNOWLEDGEMENTS

Device fabrication was performed at the Center for Integrated Nanotechnologies, an Office of Science User Facility operated for the U.S. Department of Energy (DOE) Office of Science. We are grateful to many people inside and outside Sandia for their support and fruitful collaborations.

This report describes objective technical results and analysis. Any subjective views or opinions that might be expressed in the paper do not necessarily represent the views of the U.S. Department of Energy or the United States Government.

Sandia National Laboratories is a multimission laboratory managed and operated by National Technology & Engineering Solutions of Sandia, LLC, a wholly owned subsidiary of Honeywell International Inc., for the U.S. Department of Energy's National Nuclear Security Administration under contract DE-NA0003525.

CONTENTS

This page left blank

1. INTRODUCTION

A single photon detector (SPD) can register a quantum object at an extremely minuscule energy scale, for example on the order of 10^{-23} joule for a 10 GHz microwave photon. It has found increasingly important applications in many forefront areas of fundamental science and advanced engineering, ranging from studying the galaxy formation through the cosmic infrared background to entanglement of superconducting qubits, single molecular spectroscopy, and remote sensing. Most existing SPD's are simple click detectors and can only detect either zero or more than zero photons in a multiplexed configuration, being incapable to provide deterministic photon number resolution of a light source. To solve this long-standing problem, a radically new approach is required for high-speed deterministic photon-number-resolving SPD particularly in the infrared and microwave frequency range.

We have explored in this LDRD project a new approach to SPD in an effort to provide deterministic photon-number-resolving capability by using topological Josephson junction (JJ) structures. In this SAND report, we will present results from our experimental studies of microwave response and theoretical simulations of microwave photon number resolving detector in topological Dirac semimetal Cd_3As_2. These results are promising for SPD at the microwave frequencies using topological quantum materials. As a result, nine new peer reviewed publications were generated (with three additional manuscripts under review) during this LDRD, highlighting the importance of this field of study.

2. MICROWAVE RESPONSE IN A TOPOLOGICAL SUPERCONDUCTING QUANTUM INTERFERENCE DEVICE

SPD has found increasingly important applications in many forefront areas of fundamental science and advanced engineering applications, ranging from studying the galaxy formation though cosmic infrared background to entanglement of superconducting qubits, single molecular spectroscopy, and remote sensing [1,2]. In recent years, the rapid developments in superconducting quantum computation, high fidelity quantum measurement, quantum key distribution, and quantum network call for SPD in the microwave frequency range [3]. The current SPD scheme has good sensitivity for photons in the high frequencies range (e.g., visible light). However, their sensitivity decreases drastically for low-frequency, low energy, microwave photons. As a result, the detection of single photons at this low frequency is highly prone to error from classical noise.

Graphene single photon detectors (i.e., graphene superconducting JJs) have emerged as one new platform to meet the needs of detecting single microwave photons [4,5]. It is capable of performing SPD over a wide frequency range, particularly at the infrared and microwave frequencies due to its linear energy dispersion relationship. Like graphene, the helical surface states in Cd_3As_2, a Dirac semimetal [6-8], also possess Dirac linear dispersion relationship. As a result, Cd_3As_2 is also sensitive to low-frequency microwave photons. Compared to graphene, Cd_3As_2 may be even more promising for microwave photon detection [9] based on the following reasons. First, a higher electron mobility has been reported. Indeed, a mobility as high as 10^7 cm^2/Vs has recently been reported in Dirac semimetal Cd_3As_2 single crystals [10]. Second, they can be readily grown by many conventional growth techniques, such as vapor transport [11], MBE (Molecular beam epitaxy) [12], PLD (pulsed laser deposition) [13] techniques; this enables their facile integration into any optical device structures, such as microwave cavities. Third, the unique electronic and optical properties in Cd_3As_2 may allow for polarization-resolved photon detection [14]. Fourth, superconductivity in Cd_3As_2 thin films [15] and the supercurrent states in Cd_3As_2-based JJs via the superconducting proximity effect [16-18] have been demonstrated, receptively. This may make the adoption of the well-developed single photon detection schemes, such as superconducting nanowires and transition edge sensors [2], possible in the Cd_3As_2

material system. Final, the helical surface states in topological semimetals, when combined with conventional superconductors, can host Majorana zero modes, which can be used to construct topological qubits. New single photon detection scheme utilizing Majorana zero modes have also been proposed recently [19]. Together, the microwave single photon detection capability and qubit operation is predicted to lead to high-fidelity quantum computation [20].

In this section, microwave response in this proximity induced superconducting state is presented in a superconducting quantum interference device (SQUID) structure fabricated on Cd_3As_2, as shown in the inset of Figure 1(a). In our SQUID device, a large photo response is observed at various microwave frequencies ranging from 0.5 to 10 GHz. Our results are published in Scientific Reports 11, 8615 (2021).

Device and Methods:

The mechanical exfoliation method is used to obtain flat and shiny Cd_3As_2 thin flakes from the initial bulk ingot materials. Information about the Cd_3As_2 polycrystalline ingots can be found in Ref. [16]. The thickness of the resulting exfoliated Cd_3As_2 flakes is approximately 200nm. To fabricate the alminimum-Cd_3As_2-almuninum SQUID, a two-step process is employed. First, a Cd_3As_2 flake is deposited on a Si/SiO_2 substrate (with SiO_2 thickness of 1 μm). Then, e-beam lithography is used to define the aluminum (Al) electrodes. The thickness of resultant Al electrodes is 300 nm. A low-frequency (~ 11 Hz) phase-sensitive lock-in amplifier technique, with an excitation current of 10 nA, is used to measure the sample resistance. To measure the differential resistance, a large direct current (up to ± 2μA) is added to the 10 nA *a.c.* current. The entire device is immersed in cryogenic liquid; all measurements are carried out at the cryogenic temperature of ~ 0.25K.

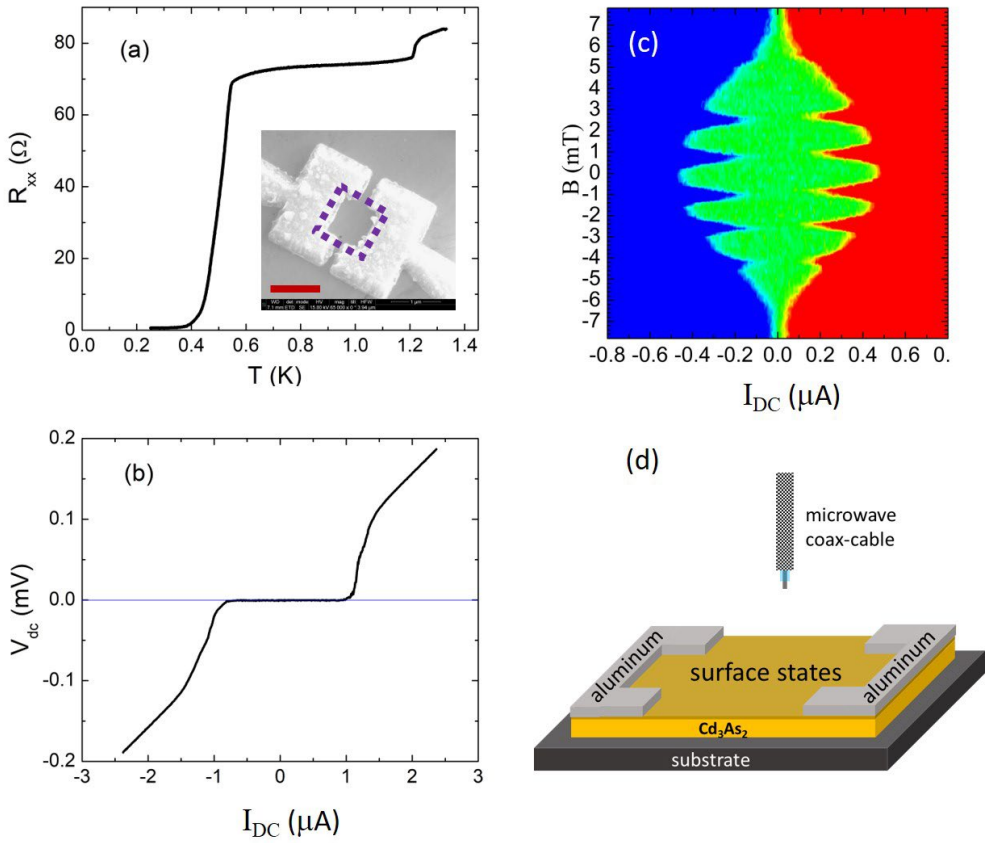

Figure 1: (a) The temperature dependence of the junction resistance in a superconducting quantum interference device (SQUID). The insert shows the SQUID device fabricated on a Cd3As2 thin flake. Th scale bar is 1 μm. (b) The current-voltage (I-V) curve measured in the SQUID. The critical current is ~ 1 μ A. (c) The two-dimensional color plot of I-V traces as a function of magnetic fields at 0.44K. The red color represents a positive Vdc, blue for negative Vdc. The green area represents the supercurrent regime. (d) The schematic setup (dimension not to scale) used to examine microwave response

Results and Discussion:

Figure 1a shows the temperature dependence of the SQUID resistance R_{xx}. At high temperatures, the R_{xx} is nearly constant. The drop at T ~ 1.2K is due to the onset of the superconductivity in the aluminum electrodes. R_{xx} continues to decrease slowly from 1.2K to ~ 0.55K. After 0.55K, R_{xx} drops precipitately and reaches a zero-resistance state at T ~ 0.35K. We thus take 0.55K as the superconducting transition temperature (T_c). Direct current-voltage (I-V) measurements in this junction is shown in Figure 1b. For large *d.c.* currents I_{DC}, the I-V curve follows a linear dependence. From the slope of this straight line, a normal state resistance of $R_n \approx 75\ \Omega$ can be deduced. Extrapolating the line to zero V_{dc}, we obtain an excess current of ~ 0.08 μA. Assuming the two JJs in the SQUID are identical and taking into account the superconducting gap of Δ =

$1.75k_BT_c$, we can estimate the barrier strength Z ~ 1 in our SQUID, based on the calculations in the paper by Flensberg et al [21,22]. Correspondingly, the junction transparency $T = 1/(1+Z^2)$ is estimated to be ~ 0.5. In the small I_{DC} regime of $|I_{DC}| < 1$ μA, the voltage across the junction V_{dc} is zero, demonstrating the robust supercurrent states. The critical current is approximately 1μA.

Figure 1c shows the magnetic field dependence of the I-V data in this SQUID. Periodic oscillations of the critical current are clearly seen, as expected for a conventional SQUID. The period is estimated to be ~ 1.8 mT. This corresponds to an effective SQUID area of ~ 1.1 μm^2, as illustrated by the dashed square in the inset of Fig. 1a. We note that in a small SQUID the effective area is often larger than the middle open area, due to the flux compression effect by the surrounding electrodes [23]. Another feature in Fig. 1c is the envelop of the oscillatory pattern being modulated by the Fraunhofer diffraction pattern of the single JJ in the SQUID.

To examine the microwave response in our SQUID device, a setup shown schematically in Figure 1d is utilized. An Agilent 83592B sweep generator is used to generate microwave photons, which are conducted through a semirigid coax cable. The end of coax cable is located about 5 mm above the sample surface. The microwave power is tuned at room temperature; the exact microwave power at the end of coax cable is not known.

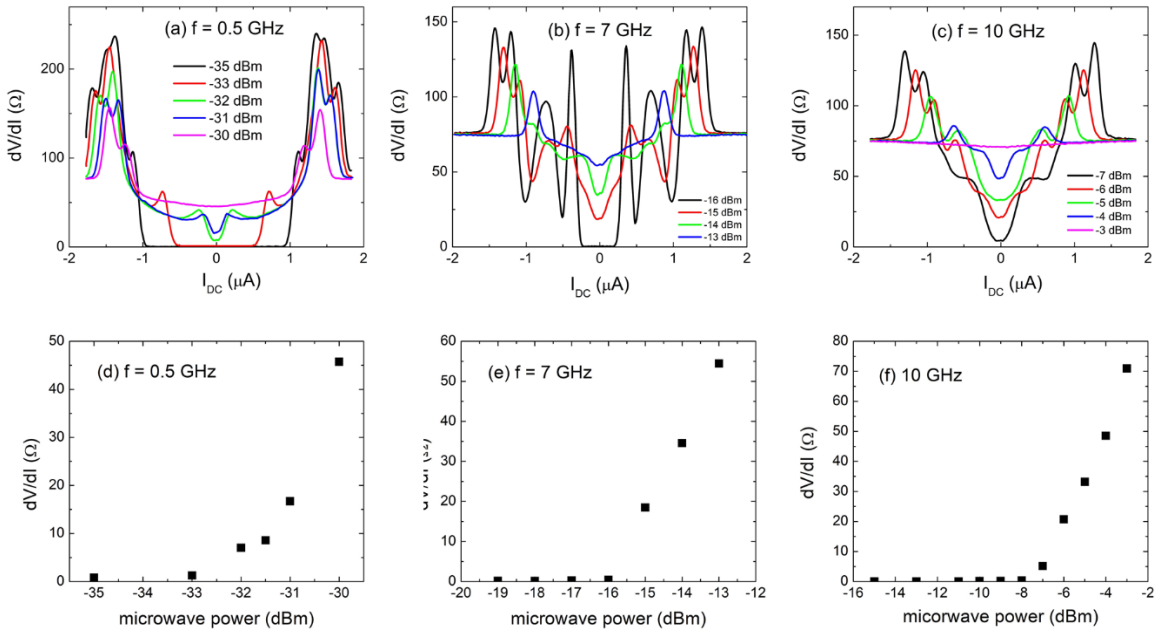

Figure 2: (a)-(c) The differential resistance measured at three selected microwave frequencies, 0.5, 7, and 10 GHz. At each frequency, the microwave power is also varied. (d)-(f) The zero-bias resistance as function of microwave power at 0.5, 7, 10 GHz, respectively.

The differential resistance dV/dI as a function of *d.c.* current bias (I_{DC}) in this SQUID is measured and reported in Figures 2a, 2b, and 2c; it has been collected at the three selected microwave frequencies of 0.5, 7, and 10 GHz, respectively. Additionally, the microwave power was varied at each frequency. The SQUID shows a large response at both the zero and also the finite *d.c.* bias. In this paper, we will focus on the microwave response at the zero-bias current. Other features, such as the Shapiro steps [24] at non-zero *d.c.* bias, merits more detailed studies and will be discussed elsewhere.

A general trend is seen when the resistance as a function of microwave power for each microwave frequency is plotted, see Figures 2d-f. At low microwave powers, the resistance is approximately zero. With further increase in microwave power, resistance becomes non-zero and starts increasing. We note here that the onset microwave power (in dBm) for non-zero dV/dI is different for different microwave frequencies, e.g., -33 dBm for f = 0.5 GHz and -16 dBm for f = 7 GHz. This is mainly due to different power attenuations at different frequencies through the semi-rigid coax cable we used in the measurements.

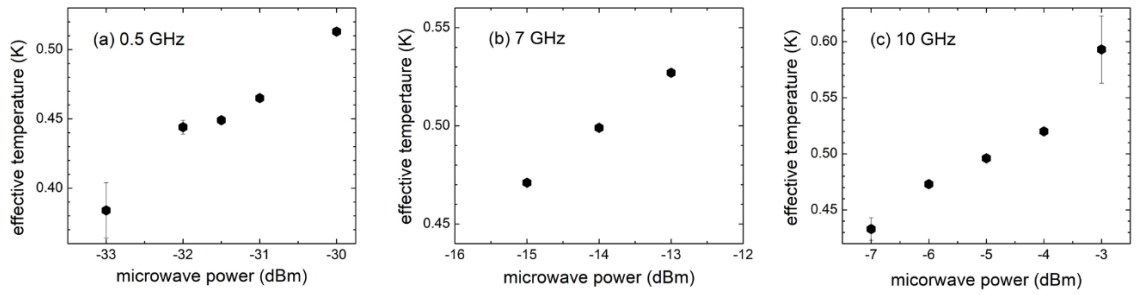

Figure 3: The effective junction temperature as a function of microwave power at 0.5 (a), 7 (b), and 10 (c) GHz.

Overall, the microwave power dependence of the zero-bias resistance shows a similar trend to its temperature dependence, seen in Fig. 1a. The zero-bias resistance is zero at low microwave powers (versus zero resistance at low temperatures). After an onset microwave power, the zero-bias resistance increases with increasing microwave power. This, again, is like the temperature dependence, in which the resistance increases with increasing temperature after a critical temperature. The similarity suggests that the increase of zero bias resistance probably is of a

bolometric origin, *i.e.* due to the increasing temperature upon microwave photon absorption. Based on this assumption, it is possible to deduce the effective electron temperature at various microwave powers by relating the resistance value with the temperature dependence from Fig. 1a.

It is important to note that this procedure works well for mid-range microwave powers, where the resistance is finite and has not reached the normal state resistance. For lower microwave powers, the resistance is zero thereby rendering it difficult to determine the effective electron temperatures. For higher microwave powers, or higher electron temperatures, the resistance change is gradual, and the error bar is relatively large. In Figure 3, a plot shows the effective electron temperature as a function of mid-range microwave power (in a logarithmic scale). It is clearly shown that the effective temperature increases roughly linearly with increasing microwave power (in the logarithmic scale).

The above result, i.e., effective temperature increasing with increasing photon energy, is promising for microwave photon detection. Indeed, with further optimization of microwave coupling structure, for example through utilization of a meander line [25], quarter wave resonator [4], or log periodic antennas [26], measurements can be done at much lower microwave power level, which may provide more support for single photon detection with number resolving [9, 27] capability. Compared to other superconducting photon detectors, such as transition edge sensors (TESs), the photon detection in this device is done by the zero-bias resistance, thus avoiding a large source-drain current needed, for example, in a TES structure [28]. Consequently, issues caused by the large source-drain current, such as the flicker noise, are greatly reduced.

Conclusion:

In summary, a large microwave response has been observed in a superconducting quantum interference device fabricated on Dirac semimetal Cd_3As_2 thin flakes, in which the temperature dependence and microwave power dependence of the junction resistance are studied. The effective temperature of the junction device under microwave radiation increases with increasing

microwave power (in the logarithmic scale). This result may pave the way of single photon detection at the microwave frequency in topological quantum materials.

REFERENCES

[1] Hadfield, H.R. Single-photon detectors for optical quantum information applications. Nature Photonics 3, 696 (2009).

[2] Eisaman, M.D., Fan, J., Migdall, A. & Polyakov, S.V. Invited Review Article: Single-photon sources and detectors. Rev. Sci. Instrum. 82, 071101 (2011).

[3] Kurpiers, P., Magnard, P., Walter, T., Royer, B., Pechal, M., Heinsoo, J., Salathé, Y., Akin, A., Storz, S., Besse, J.-C., Gasparinetti, S., Blais & Wallraff, A. Deterministic quantum state transfer and remote entanglement using microwave photons. Nature 558, 264 (2018).

[4] Walsh, E.D., Efetov, D.K., Lee, G.-H., Heuck, M., Crossno, J., Ohki, T.A., Kim, P., Englund, D. & Fong, K.C. Graphene-Based Josephson-Junction Single-Photon Detector. Phys. Rev. Applied 8, 024022 (2017).

[5] Koppens, F.H.L., Mueller, T., Avouris, Ph., Ferrari, A.C., Vitiello, M.S. & Polini, M. Photodetectors based on graphene, other two-dimensional materials and hybrid systems. Nature Nanotechnology 9, 780 (2014).

[6] Young, S.M., Zaheer, S., Teo, J.C.Y., Kane, C.L., Mele, E.J. & Rappe, A.M. Dirac Semimetal in Three Dimensions. Phys. Rev. Lett. 108, 140405 (2012).

[7] Wan, X., Turner, A.M., Vishwanath, A. & Savrasov, S.Y. Topological semimetal and Fermi-arc surface states in the electronic structure of pyrochlore iridates. Physical Review B 83, 205101 (2011).

[8] Lee, S.R., Sharma, P.A., Lima-Sharma, A.L., Pan, W. & Nenoff, T.M. Topological Quantum Materials for Realizing Majorana Quasiparticles. Chem. Mater. 31, 26 (2019).

[9] Chatterjee, E., Pan, W. & Soh, D. Microwave Photon Number Resolving Detector Using the Topological Surface State of Superconducting Cadmium Arsenide. ArXiv:2009.02096 (2020).

[10] Liang, T., Gibson, Q., Ali, M.N., Liu, M., Cava, R.J. & Ong, N.P. Ultrahigh mobility and giant magnetoresistance in the Dirac semimetal Cd_3As_2. Nature Materials 14, 280 (2015).

[11] Ali, M.N., Gibson, Q., Jeon, S., Zhou, B.B., Yazdani, A. & Cava, R.J. The Crystal and Electronic Structures of Cd_3As_2, the Three-Dimensional Electronic Analogue of Graphene. Inorg. Chem. 53, 4062 (2014).

[12] Schumann, T., Galletti, L., Kealhofer, D.A., Kim, H., Goyal, M. & Stemmer, S. Observation of the Quantum Hall Effect in Confined Films of the Three-Dimensional Dirac Semimetal Cd_3As_2. Phys. Rev. Lett. 120, 016801 (2018).

[13] Uchida, M., Nakazawa, Y., Nishihaya, S., Akiba, K., Kriener, M., Kozuka, Y., Miyake, A., Taguchi, Y., Tokunaga, M., Nagaosa, N., Tokura, Y. & Kawasaki, M. Quantum Hall states observed in thin films of Dirac semimetal Cd3As2. Nature Communications 8, 2274 (2017).

[14] Conte, A.M., Pulci, O. & Bechstedt, F. Electronic and optical properties of topological semimetal Cd_3As_2. Scientific Report 7: 45500 (2017).

[15] Oveshnikov, L.N., Davydov, A.B., Suslov,A.V., Ril', A.I., Marenkin, S.F., Vasiliev, A.L. & Aronzon, B.A. Superconductivity and Shubnikov - de Haas effect in polycrystalline Cd_3As_2 thin films, Scientific Reports 10: 4601 (2020).

[16] Yu, W., Pan, W., Medlin, D.L., Rodriguez, M.A., Lee, S.R., Bao, Z.-Q. & Zhang, F. π and 4π Josephson Effects Mediated by a Dirac Semimetal. Phys. Rev. Lett. 120, 177704 (2018).

[17] Wang, A.-Q., Li, C.-Z., Li, C., Liao, Z.-M., Brinkman, A. & Yu, D.-P. 4π-Periodic Supercurrent from Surface States in Cd_3As_2 Nanowire-Based Josephson Junctions. Phys. Rev. Lett. 121, 237701 (2018).

[18] Yu, W., Haenel, R., Rodriguez, M.A., Lee, S.R., Zhang, F., Franz, M., Pikulin, D.I. & Pan, W. Zero-bias conductance peak in Dirac semimetal-superconductor devices. Phys. Rev. Research 2, 032002 (2020).

[19] Chi, F., He, T.-Y., Wang, J., Fu, Z.-G., Liu, L.-M., Liu, P. & Zhang, P. Photon-Assisted Transport Through a Quantum Dot Side-Coupled to Majorana Bound States. Front. Physics 8, 254 (2020).

[20] Opremcak, A., Pechenezhskiy, I.V., Howington, C., Christensen, B.G., Beck, M.A., Leonard Jr., E., Suttle, J., Wilen, C., Nesterov, K.N., Ribeill, G.J., Thorbeck, T., Schlenker, F., Vavilov. M.G., Plourde, B.L.T. & McDermott, R. Measurement of a superconducting qubit with a microwave photon counter. Science 361, 1239-1242 (2018).

[21] Flensberg, F., Hansen, J.B. & Octavio, M. P Subharmonic energy-gap structure in superconducting weak links. Phys. Rev. B 38, 8707 (1988).

[22] Bai, M., Yang, F., Luysberg, M., Feng, J., Bliesener, A., Lippertz, G., Taskin, A.A., Mayer, M. & Ando, Y. Novel self-epitaxy for inducing superconductivity in the topological insulator $(Bi_{1-x}Sb_x)_2Te_3$, Phys. Rev. Materials 4, 094801 (2020).

[23] Qu, F., Yang, F., Shen, J., Ding, Y., Chen, J., Ji, Z., Liu, G., Fan, J., Jing, X., Yang, C. & Lu, L. Strong Superconducting Proximity Effect in Pb-Bi_2Te_3 Hybrid Structures. Sci. Rep. 2, 339 (2012).

[24] Michael Tinkham, Introduction to superconductivity, McGraw-Hill, New York, NY, USA 1996.

[25] Ye, P.D., Engel, L.W., Tsui, D.C., Lewis, R.M., Pfeiffer, L.N. & West, K. Correlation Lengths of the Wigner-Crystal Order in a Two-Dimensional Electron System at High Magnetic Fields. Phys. Rev. Lett. 89, 176802 (2002).

[26] Dyer, G.C., Aizin, G.R., Preu, S., Vinh, N.Q., Allen, S.J., Reno, J.L. & Shaner, E.A. Inducing an Incipient Terahertz Finite Plasmonic Crystal in Coupled Two Dimensional Plasmonic Cavities. Phys. Rev. Lett. 109, 126803 (2012).

[27] Roy, K., Ahmed, T., Dubey, H., Sai, T.P., Kashid, R., Maliakal, S., Hsieh, K., Shamim, S. & Ghosh, A. Number-Resolved Single-Photon Detection with Ultralow Noise van der Waals Hybrid. Adv. Mater. 30, 1704412 (2018).

[28] Gerrits, T., Calkins, B., Tomlin, N., Lita, A.E., Migdall, A., Mirin, R. & Nam, S.W. Extending single-photon optimized superconducting transition edge sensors beyond the single-photon counting regime. Optical Express 20, 23798 (2012).

3. MICROWAVE PHOTON NUMBER RESOLVING DETECTOR USING THE TOPOLOGICAL SURFACE STATE OF SUPERCONDUCTING CADMIUM ARSENIDE

I. INTRODUCTION

Photon number resolving detectors have been explored significantly over the past decades [1-3] due to the dire need for resolving the number of photons in applications such as the security of quantum communications [4, 5] and the sensitivity of quantum sensing [6]. As photon-based quantum computing advances, precise resolution of photon number detection is increasingly important. Microwave photons are the backbone of prolific transmon quantum computation, and therefore, detection of the microwave photons is tremendously important in the current quantum computing paradigm [7]. Several non-number-resolving techniques to detect microwave photons have been developed, including the circuit QED technique [8], dressed-state superconducting quantum circuit [9], current-biased JJ [10], and the dark-state detector [11]. It is well-known that building a parallel detection system, first splitting the light path using beam splitters and then using non-number-resolving detectors in each parallel path, may provide a probabilistic photon number resolving detection, which is further limited due to the loss associated with parallelization. In contrast, a single photon-number resolving detector with a deterministic photon number resolution would provide a immense advantage particularly in photonic quantum computers by reducing the error-correcting overhead. To the best of our knowledge, a single-device photon-number resolving detector that can simultaneously detect multiple incoming photons at microwave frequency has not been reported so far.

Here, we propose a photon-number resolving detector operating at microwave frequencies, based on the topological surface states of cadmium arsenide (Cd_3As_2). Semimetals such as graphene provide an ideal detecting material for microwave photons due to their zero band gap. Recently, Dirac and Weyl semimetals with Dirac cone dispersion have gained prominence due to high mobility [12], along with the fact that they can be synthesized through conventional techniques [13-15]. Particularly, Cd_3As_2 displays proximity-induced bulk superconductivity at low temperatures, and the electronic structures of the bulk and the topological surface states are decoupled. Maintaining the Cd_3As_2 semimetal material at a very low temperature is necessary for an efficient photon-induced electron excitation to a conduction band just above the Fermi level

due to the low photon energy. The bulk state enters a superconducting state at a sufficiently low temperature, opening a band gap beyond the microwave photon energy. Fortunately, the topological surface state of Cd_3As_2 is not affected by the temperature, continuing to provide a gapless Dirac cone. We use this topological surface state as a photon absorber. Once the photon is absorbed, a rapid rethermalization in band population occurs with a new elevated temperature corresponding to the absorbed photon energy. We then utilize the fact that the redistributed electron population transfers its energy to the bulk's phonon modes via a surface electron-bulk phonon coupling, thus increasing the bulk's temperature. The elevated bulk temperature then reduces the conductance of the superconducting bulk electron state, which is measured and used to eventually indicate the number of photons absorbed. Results are published in Phys. Rev. Research 3, 023046 (2021).

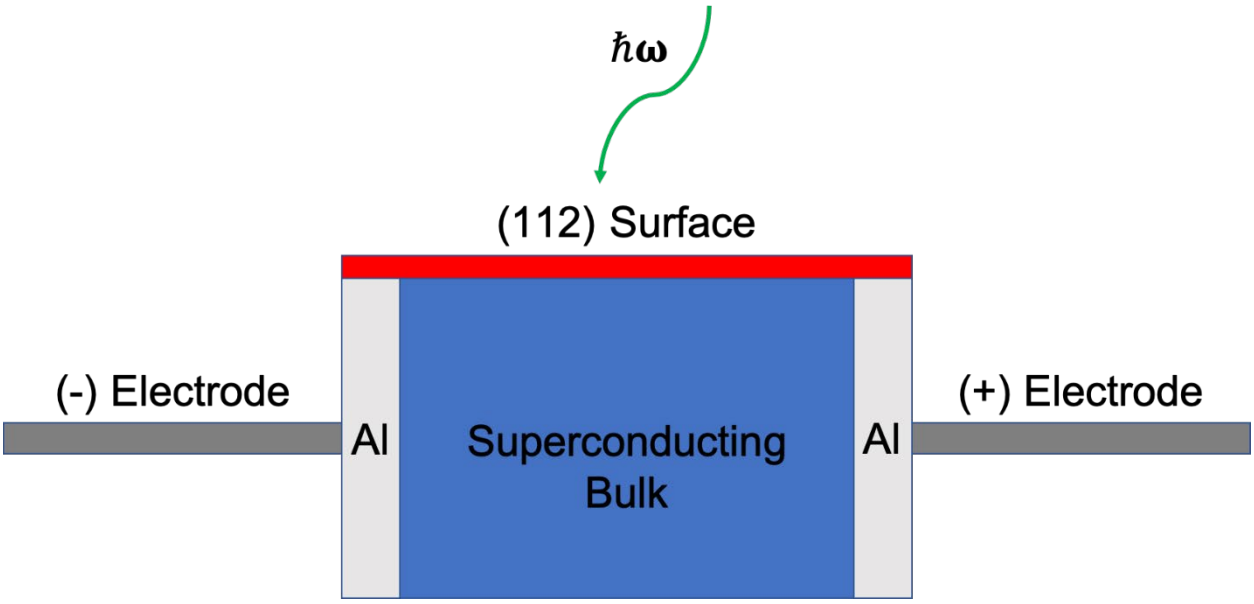

Figure 1: Basic layout for the Cd_3As_2 photon number resolving device. At low temperatures, the bulk becomes superconducting due to the material's proximity to superconducting aluminum, while the (112) surface retains a graphene-like dispersion. A photon (depicted by the arrow) is absorbed by the surface electrons. The change in bulk resistivity (measured by the electrodes at zero bias) is used to determine the temperature increase. Note that the Al bars are positioned in the out-of-plane direction with respect to the Cd_3As_2 material.

II. PHOTON ABSORPTION IN TOPOLOGICAL SURFACE STATE

The setup for the device is depicted in Fig. 1. The system is based on a Cd_3As_2 crystal inside a low-temperature refrigerator with a baseline temperature below the bulk superconducting critical

temperature. Recent experimental findings have demonstrated that Cd_3As_2 features a topological surface state on the (112) surface with a linear band crossing around the Dirac points [16, 17]. This graphene-like surface state band structure at low energy can be attributed to the fact that sites consisting of stacked As and Cd atoms approximately form a honeycomb superlattice on the (112) surface [13]. As with graphene, the dispersion relationship can be expressed as the following linear function of the wavevector k when the Fermi level is at the Dirac point:

$$E_{c,v}(\boldsymbol{k}) = \pm \hbar v_F |\boldsymbol{k}|, \qquad (1)$$

where ħ is the Planck constant, c and v represent the conduction and valence bands, respectively, and vF denotes the Fermi velocity, which is approximately 10^6 m/s. [16, 18]. At low temperatures, if the material is in proximity to superconducting aluminum (Al), the surface state electrons are decoupled from the bulk state, and the bulk becomes superconducting below 0.7 K while the surface retains its semimetallic property [19]. We measure the superconducting gap frequency f_{gap} near zero temperature (T = 21 mK) and at T = 0.39 K from Figs. 2(a) and 1(d) of Yu et al. [19]. For the case of near-zero temperature, the gap is measured as 0.113 meV (corresponding to a frequency of 27 GHz), while at 0.39 K, the gap amounts to 0.088 meV (corresponding to 21 GHz). The resulting band structures for the superconducting bulk and the topological surface state are compared in Fig. 2. Note that this proximity-induced superconducting gap is smaller than the gap predicted from BCS theory [20], which would equal about 50 GHz for a critical temperature around 0.7 K. Nonetheless, even for temperatures as high as 0.35-0.45 K, photons of microwave frequency below approximately 20 GHz will be absorbed solely by the surface state. Since we are primarily interested in microwave photons of frequency 5-10 GHz, this satisfies our goal of using the surface as the absorber and the bulk as the thermometer.

In order to derive the absorption probability, we consider the physical manifestation of the Dirac cone on the nature of the Bloch states. As in graphene, each electronic state in the vicinity of a Dirac point can be conceptualized as a massless Dirac fermion with a well-defined momentum ħk, where k represents the wavevector of the electronic state in the reciprocal space for which the

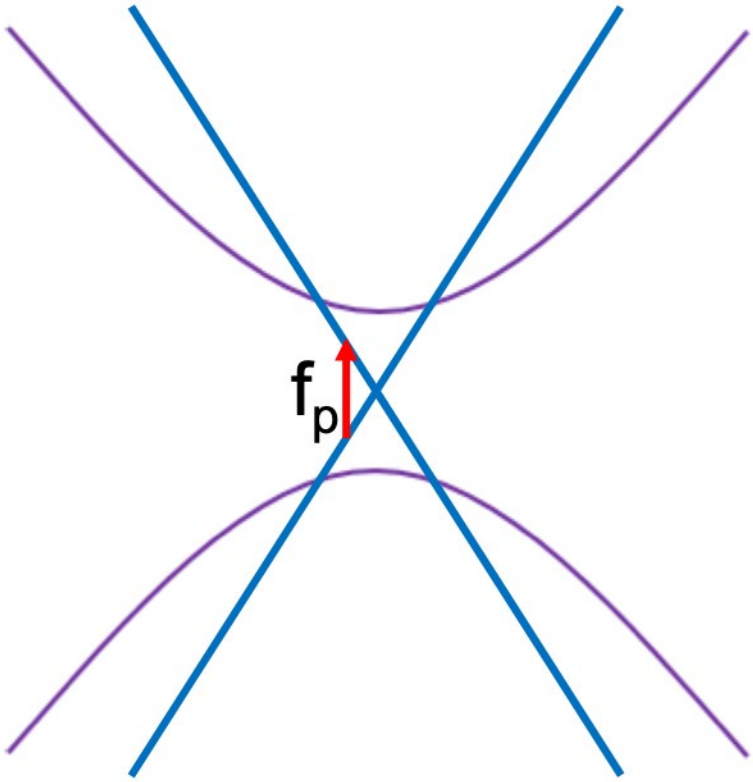

Figure2: Band structures for the superconducting bulk (purple curves) and the topological surface state (blue straight lines). Note that a gap of frequency f_{gap} is opened in the bulk, while the surface state remains gapless, thus restricting the absorption of photons at microwave frequency f_p to the surface state.

Dirac point is the origin. Therefore, the absorption coefficient for Cd_3As_2 will equal the corresponding value for graphene [21]:

$$A(\omega) = \frac{e^2}{4\hbar\epsilon_0 c}\left(f\left(-\frac{\hbar\omega}{2}, T\right) - f\left(\frac{\hbar\omega}{2}, T\right)\right) \\ = \frac{e^2}{4\hbar\epsilon_0 c}\tanh\left(\frac{\hbar\omega}{4k_B T}\right), \quad (2)$$

where e is the charge of an electron, ε_0 is the vacuum permittivity, c the speed of light, and f(E;T) denotes the Fermi-Dirac electron occupation probability at energy E for temperature T. Note that the absorption coefficient (as a function of photon frequency) is invariant with respect to the Fermi velocity. This is because the interband dipole matrix element (corresponding to the

absorption probability for a single electronic state) increases with the Fermi velocity, while the density of states decreases with it, eventually canceling each other's effect. At high frequencies ($\hbar\omega >> k_BT$), the absorption coefficient (i.e., the quantum efficiency for a single pass through a single Cd_3As_2 crystal) is approximately invariant with frequency, equaling a constant value of $e^2/(4\hbar\varepsilon_0 c) = 2.3\%$. On the other hand, at low frequencies on the scale $\hbar\omega \leq kBT$, the coefficient becomes attenuated, reaching a minimum value of zero as the Dirac cone is approached. We will use an upper bound base-line temperature of 0.45 K, which will set the minimum quantum efficiency for photons of a given frequency interacting with a single crystal. For microwave frequencies ranging from 5-10 GHz, Eq. (2) implies a single-crystal quantum efficiency ranging from 0.3-0.6%. build credible real use cases of the proposed scheme. In the final section, we summarize our results and suggest the path toward building a photon-number resolving detector with near-unity efficiency on a chip.

III. TEMPERATURE INCREASE VS. ABSORBED PHOTON NUMBER

Having determined the probability that the topological surface state absorbs a photon from an incoming field, our next step is to determine how the absorption of a single photon increases the temperature of the 3D bulk sample. When a photon excites an electron to the conduction band, a rapid rethermalization of the Fermi-Dirac distribution through electron-electron interaction ensues, leading to an electron temperature above the lattice temperature. For undoped monolayer graphene, which features a band structure approximately identical to that for the Cd3As2 surface state, this process occurs in tens of picoseconds for cryogenic baseline temperatures [22]. The carrier rethermalization is followed by heat transfer from the collection of electrons to the lattice via electron-acoustic phonon interaction, until a thermal equilibrium is reached between the electron temperature and the lattice temperature. Generally, the interaction between electrons and acoustic phonons is much slower than the electron-electron interaction [23-25]. Afterward, the Fermi-Dirac distribution for the electron bands and the Bose-Einstein distribution for the phonon branches will comply with the same temperature.

We now determine the temperature increase due to the absorption of a photon of frequency ω by calculating the portion of the imparted energy that is eventually converted to bulk lattice vibrations (i.e., the phonon modes) and to the surface electron modes, and by deriving the heat

capacity of the two systems. We will make two important assumptions here: first, that the electron-electron interaction rate dominates over the radiative loss rate of the electrons (which we will demonstrate in a later section), and second, that the very low values for the initial and final temperatures ensure that virtually all of the phonons are located in the low-energy linear parts of the acoustic branches, thus allowing for use of the Debye approximation [26] in determining the heat capacity.

A. Energy Gain for Surface Electron Modes: We start by writing out an expression corresponding to energy conservation in the system given the absorption of a photon of frequency ω:

$$\hbar\omega = \Delta U_{el} + \Delta U_{ph}, \tag{3}$$

where ΔU_{el} and ΔU_{ph} represent the total energy gained by the topological surface electron modes and the bulk phonon modes, respectively, at equilibrium. We focus first on the energy gain for the electron modes as a function of electron temperature, as this will be necessary for calculating the initial electron temperature gain after photon absorption but prior to heat transfer to the lattice. The total electron energy with respect to the Fermi sea is calculated by taking a sum of the conduction and valence band energies weighted by the Fermi-Dirac occupation probabilities (multiplied by 2 to account for the fact that each spatial state contains 2 spin states):

$$U_{el}(T) = 2\sum_{\boldsymbol{k}} \left(E_{c,\boldsymbol{k}} f(E_{c,\boldsymbol{k}}, T) - E_{v,\boldsymbol{k}} \Big(1 - f(E_{v,\boldsymbol{k}}, T)\Big) \right). \tag{4}$$

The first term corresponds to the energy gained in creating a conduction band electron, while the second term corresponds to the energy gained in creating a valence band hole. Since the deviation from the Fermi sea at low temperatures is concentrated in the vicinity of the Dirac cone, we can assume that the linear isotropic dispersion relationship in Eq. (1)

holds for the entire relevant wavevector range. Therefore, the summation over wavevectors can be replaced by an integral over the density of spatial states (ρ_c and ρ_v for the conduction and valence bands, respectively):

$$U_{el}(T) = 2\int_0^{-\infty} dE_v \rho_v(E_v)(-E_v)\left(1 - \frac{1}{e^{\frac{E_v}{k_B T}} + 1}\right) + 2\int_0^{\infty} dE_c \rho_c(E_c) E_c \frac{1}{e^{\frac{E_c}{k_B T}} + 1}. \tag{5}$$

Since the conduction and valence band energies are opposite at each wavevector, we can express Uel as a single integral over the energy absolute value E, where $E_c = E$ and $E_v = -E$. Due to the equivalent magnitudes of the dispersion slope for the conduction and valence bands at each wavevector, we can further define a general density of states $\rho(E) = \rho_v(E) = \rho_c(E)$:

$$\begin{aligned} U_{el}(T) &= 2\int_0^{\infty} dE \rho(E) E\left(1 - \frac{1}{e^{-\frac{E}{k_B T}} + 1}\right) \\ &\quad + 2\int_0^{\infty} dE \rho(E) E \frac{1}{e^{\frac{E}{k_B T}} + 1} \\ &= 2\int_0^{\infty} dE \rho(E) E \frac{e^{-\frac{E}{k_B T}} + 1}{\cosh\left(\frac{E}{k_B T}\right) + 1}. \end{aligned} \tag{6}$$

The density of states at band energy E can be solved by applying the dispersion relationship as follows:

$$\begin{aligned}\rho(E) &= \frac{dN}{dA_k}\frac{dA_k}{dk}\frac{dk}{dE} \\ &= \frac{A}{(2\pi)^2}\left(2\pi\frac{E}{\hbar v_F}\right)\frac{1}{\hbar v_F} \\ &= \frac{A}{2\pi\hbar^2 v_F^2}E,\end{aligned} \tag{7}$$

where A is the surface state area, Ak is the area in the reciprocal space associated with the value k = |k|, and N is the number of states. As expected for the graphene-like band structure, the density of states is linear in the energy. We are thus in a position to solve for the electron energy $U_{el}(T)$ as a function of temperature T:

$$\begin{aligned}U_{el}(T) &= \frac{A}{\pi\hbar^2 v_F^2}\int_0^\infty dE E^2 \frac{e^{-\frac{E}{k_B T}}+1}{\cosh\left(\frac{E}{k_B T}\right)+1} \\ &= \frac{A}{\pi\hbar^2 v_F^2}3(k_B T)^3\zeta(3),\end{aligned} \tag{8}$$

where ζ represents the Riemann zeta function, with ζ(3) ≈ 1.2. This implies that the electron temperature varies with the total electron energy as $U_{el}^{1/3}$, and the relationship between the gain in electron energy and the temperature change from T_i to T_f takes the following form:

$$\Delta U_{el} = \frac{3.6Ak_B^3}{\pi\hbar^2 v_F^2}\left(T_f^3 - T_i^3\right). \tag{9}$$

For detecting a moderate number of microwave photons, we are primarily interested in the limit $\Delta T(\equiv T_f - T_i) << T_i$ where Ti > 0.1 K. In that limit, the cooling power Q for the electron modes is related to the rate of change of the temperature by taking the derivative of ΔU_{el} with respect to time, yielding the following function of the temperature T ≈ Ti:

$$Q = -\frac{d}{dt}\left(\frac{3.6Ak_B^3}{\pi\hbar^2 v_F^2}T^3\right) = -\frac{10.8Ak_B^3}{\pi\hbar^2 v_F^2}T^2\frac{dT}{dt}. \qquad (10)$$

B. Energy Gain for Bulk Phonon Modes: Next, we look to determine how the energy gained by the lattice vibrations relates to the lattice temperature. In general, the total phonon energy is determined as a function of temperature by summing over the modes corresponding to various phonon branches μ and phonon wavevectors q, weighted by the occupation number $\langle n_{\mu,q} \rangle$ for each phonon mode:

$$U_{ph}(T) = \sum_{\mu}\sum_{\boldsymbol{q}} \langle n_{\mu,\boldsymbol{q}}(T)\rangle \, \hbar\omega_{\mu,\boldsymbol{q}}, \qquad (11)$$

where $\mu_{\mu,q}$ is the frequency of the phonon mode of branch μ and wavevector q, and the occupation number at a given temperature T is calculated from the Bose-Einstein distribution:

$$\langle n_{\mu,\boldsymbol{q}}(T)\rangle = \frac{1}{e^{\frac{\hbar\omega_{\mu,\boldsymbol{q}}}{k_B T}} - 1}. \qquad (12)$$

As previously mentioned, the fact that the sample is in the low-temperature regime (below 0.5 K) indicates that the Debye model, with its assumption of a linear phonon dispersion, is approximately valid for the phonon modes with non-negligible occupation numbers. Therefore, we can restrict the summation over branches to just the 3 acoustic branches (corresponding to the 3 polarizations). In general, the slope of each of these branches is slightly anisotropic in reciprocal space due to the varying angle between the polarization and propagation directions. However, per the treatment in Kittel [27], we can approximate the composite effect of the 3 branches on the summation in Eq. (11) as equivalent to a summation over 3 isotropic branches, each featuring a slope of vs (i.e., the

speed of sound in the material), such that:

$$U_{ph}(T) = 3\sum_{\boldsymbol{q}} \frac{\hbar\omega_q}{e^{\frac{\hbar\omega_q}{k_B T}} - 1}, \qquad (13)$$

where $\omega_q = v_s q$, and the speed of sound v_s for Cd_3As_2 is estimated as 2.3 x 10^3 m/s [25].

We now replace the summation over wavevectors with an integral over the density of states for each branch in terms of frequency, D(ω). For a 3-dimensional lattice with a speed of sound v_s, this density is determined as follows:

$$\begin{aligned} D(\omega) &= \frac{dN}{dV_q}\frac{dV_q}{dq}\frac{dq}{d\omega} \\ &= \frac{V}{(2\pi)^3}\left(4\pi\left(\frac{\omega}{v_s}\right)^2\right)\frac{1}{v_s} \\ &= \frac{V\omega^2}{2\pi^2 v_s^3}, \end{aligned} \qquad (14)$$

where V is the bulk volume of the lattice and V_q is the volume in the reciprocal space associated with q = |q|. We therefore solve for the total phonon energy as a function of temperature through the following integral:

$$\begin{aligned} U_{ph}(T) &= 3\int_0^\infty d\omega D(\omega)\frac{\hbar\omega}{e^{\frac{\hbar\omega}{k_B T}} - 1} \\ &= \frac{3V\hbar}{2\pi^2 v_s^3}\int_0^\infty d\omega \frac{\omega^3}{e^{\frac{\hbar\omega}{k_B T}} - 1}. \end{aligned} \qquad (15)$$

Note that the expression differs from that in Kittel in that we use ∞ instead of a specific Debye cutoff for the upper bound of the frequency range. As in the case of the integral over energy for the electronic modes in the previous section, this is justified by the rapid convergence of the integrand to 0 at very low temperatures [28], corresponding to the fact that only the linear regime of the acoustic branches are non-negligibly occupied. Then, we find the following result:

$$U_{ph}(T) = \frac{3Vk_B^4T^4}{2\pi^2 v_s^3\hbar^3}\int_0^\infty d\left(\frac{\hbar\omega}{k_BT}\right)\frac{\left(\frac{\hbar\omega}{k_BT}\right)^3}{e^{\frac{\hbar\omega}{k_BT}}-1} \qquad (16)$$
$$= \left(\frac{3Vk_B^4T^4}{2\pi^2 v_s^3\hbar^3}\right)\left(\frac{\pi^4}{15}\right)$$

Unlike the total surface electron energy, which scales as T^3, the total bulk phonon energy scales as T^4. This difference can be attributed to the fact that the surface is 2D whereas the bulk is 3D, having more degrees of freedom, thus implying that all else being equal, a given change in energy would have a weaker effect on bulk temperature than on surface temperature. The change in the total phonon energy can therefore be related to the initial and final temperatures T_i and T_f as follows:

$$\Delta U_{ph} = \frac{\pi^2 Vk_B^4}{10\hbar^3 v_s^3}\left(T_f^4 - T_i^4\right). \qquad (17)$$

Note that, for a prism-shaped sample (such as a thin film) for which the surface state forms one of the two bases for the prism, the bulk volume is proportional to the surface area as V = Ad, where d represents the sample thickness.

C. Energy Gain for Bulk Phonon Modes: Having derived the energy gain for the surface electron and the bulk phonon modes for given initial and final temperatures, we now seek to compare the specific heat values for the two mode types in order to glean an understanding of how the excess thermal energy is distributed between the modes. From

the result in Eq. (9), the specific heat for the collection of surface electrons is determined as follows:

$$C_{el}(T) = \frac{dU_{el}}{dT} = \frac{10.8Ak_B^3}{\pi\hbar^2 v_F^2}T^2. \qquad (18)$$

The specific heat for the bulk lattice is calculated in an analogous manner from the result in Eq. (17):

$$C_{ph}(T) = \frac{dU_{ph}}{dT} = \frac{2\pi^2 V k_B^4}{5\hbar^3 v_s^3}T^3. \qquad (19)$$

Using the relationship V = Ad, where d denotes the bulk depth of the lattice, we divide Eq. (19) by (18) in order to determine the ratio of the specific heat values for a given temperature:

$$\begin{aligned}\frac{C_{ph}(T)}{C_{el}(T)} &= \frac{\pi^3 k_B v_F^2}{27\hbar v_s^3}Td \\ &= \left(1.24 \times 10^{13}\ \mathrm{K^{-1}m^{-1}}\right)Td.\end{aligned} \qquad (20)$$

Since the baseline refrigerator temperature is at least 0.25K, this sets the minimum value for T. The lattice depth d must be at least multiple times longer than the lattice constant, which is 3 - 5 Å for Cd_3As_2 [29]. Therefore, the phonon specific heat is far higher than the electron specific heat (by at least 3 orders of magnitude), indicating that nearly all of the thermal energy gained from the photon absorption is eventually stored in the lattice vibrational modes. As such, if N photons of frequency ω are absorbed, then the relationship between the final equilibrium temperature T_f and the initial temperature T_i can be determined from Eq. (17):

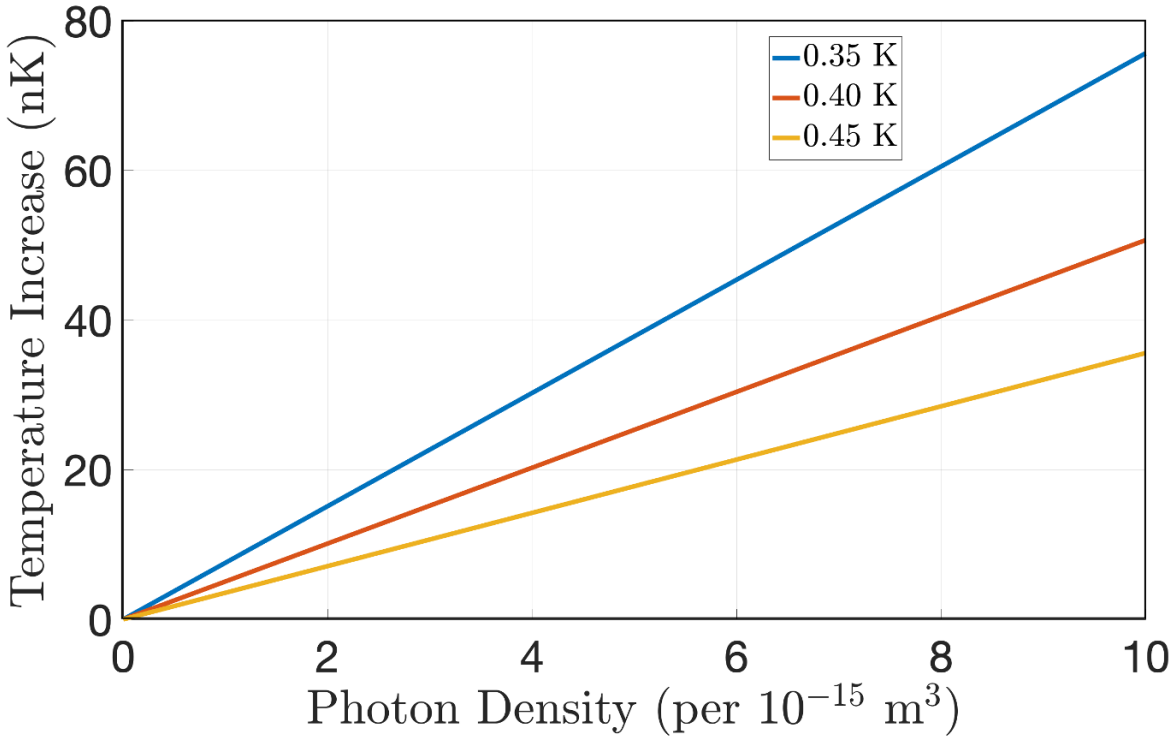

Figure 3: Plots of temperature gain (in nanokelvins) versus density of absorbed photons (per 10^{-15} m^3) for baseline temperatures Ti = 0.35; 0.40; and 0.45 K given a photon frequency f = 5 GHz.

$$T_f = \left(T_i^4 + \frac{10\hbar^3 v_s^3}{\pi^2 V k_B^4} N\hbar\omega \right)^{1/4} = \left(T_i^4 + \left(4.13 \times 10^{-35}\ \mathrm{m^3K^4s}\right) \frac{N\omega}{V} \right)^{1/4} \quad (21)$$

As this expression shows, the determinitive factor in the temperature increase is the total photon energy absorbed per unit volume of the lattice, which is proportional to Nω=V . We plot the temperature gain as a function of photoelectron density N=V for 3 different baseline temperatures 0.35 K, 0.40 K, and 0.45 K, for an input photon frequency of 5 GHz (corresponding to $\omega = \pi \times 10^{10}$ s^{-1}) in Fig. 3. Note that for low photon densities such that the temperature gain is small compared to the baseline temperature, the relationship between temperature gain and photon density is approximately linear, as expected. The imbalance between the electron and lattice specific heat values also has significant implications for the heat transfer between the electron and phonon distributions that

ultimately yields the equilibrium state. In particular, when comparing the quasiequilibrium electron and lattice temperatures to the final equilibrium temperature for the whole system, the equilibrium temperature will be much closer to the quasiequilbrium lattice temperature than to the electron temperature. We consider the timescale for the electron-lattice heat transfer as a function of temperature in the next section.

IV. ELECTRON-PHONON INTERACTION TIMESCALE

Having derived the equilibrium temperature for the bulk lattice upon photon absorption, we now aim to estimate the timescale over which that equilibrium is reached. As previously mentioned, this energy transfer takes place in two steps: a rapid electron-electron rethermalization, followed by heat transfer from the electrons to the acoustic vibrations of the lattice (which is much slower than the electron-electron interaction [23-25]). Here, we will focus on the latter process, since it serves as the limiting factor in setting the minimum timescale for reaching equilibrium. The heat transfer timescale between bulk electrons and lattice phonons in Cd_3As_2 has been the subject of recent analysis [25, 30], and here we will build on that analysis to solve for the heat transfer timescale between surface electrons and lattice phonons. We will characterize the available phase space area for bulk phonon emission by the surface electrons, derive the matrix element for the electron-phonon interaction, and finally calculate the rate for the electron-phonon heat transfer.

A. Phase Space: We start by examining the available phase space for the interaction between 2D surface state electrons and the bulk phonon modes. Unlike the spherical equal-energy manifolds for the 3D Dirac cone carrier modes, the 2D Dirac cone electron modes take a cylindrical equal-energy manifolds, with a degree of freedom in the kz-direction (corresponding to the axis perpendicular to the surface). We therefore use cylindrical coordinates, expanding the final electron wavevector p as ($p\cos\theta_p$; $\sin\theta_p$; p_z) and the initial wavevector k as (k; 0; 0). In this coordinate system the emitted phonon wavevector q can be expanded as follows:

$$\boldsymbol{q} = \boldsymbol{k} - \boldsymbol{p} = (p\cos\theta_{\boldsymbol{p}} - k, p\sin\theta_{\boldsymbol{p}}, p_z). \qquad (22)$$

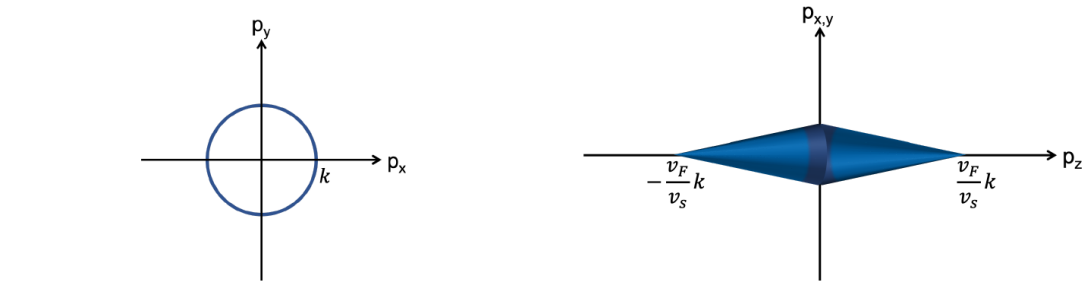

(a) (b)

Figure 4: Depiction of the phase space area of final electronic states for a given initial state k = (k; 0; 0), including the 2D cross-section of the phase space along the p_xp_y-plane (a) and the phase space along the p_z-axis (b). The phase space forms a double cone, with a base of radius k on the p_xp_y-plane, and tapering off in the $+p_z$ and $-p_z$ directions with a length of v_Fk/v_s along each. Note that the base versus height ratio for the double-cone in (b) is not to scale.

Note that the bulk phonon's equal-energy manifolds retain a 3D spherical shape defined by $w = v_sq$. We map this onto the electron's manifolds using energy conservation:

$$v_F k - v_F p = v_s \sqrt{(p\cos\theta_{\boldsymbol{p}} - k)^2 + p^2 \sin^2\theta_{\boldsymbol{p}} + p_z^2}. \quad (23)$$

Squaring both sides and solving for p, we find that p varies with both θ_p and p_z:

$$p = k\left(1 + \Delta(\theta_{\boldsymbol{p}}) - \sqrt{\left(1+\Delta(\theta_{\boldsymbol{p}})\right)^2 - 1 + \left(\frac{v_s^2}{v_F^2 - v_s^2}\right)\frac{p_z^2}{k^2}}\right), \quad (24)$$

where $\Delta(\theta_p)$ is defined as follows:

$$\Delta(\theta_{\boldsymbol{p}}) = \frac{v_F^2 - v_s^2\cos\theta_{\boldsymbol{p}}}{v_F^2 - v_s^2} - 1. \quad (25)$$

For our material, $v_s << v_F$, thus yielding $\Delta(\theta_p) << 1$ for all θ_p. Therefore, p can be approximately expressed as solely a linear function of p_z:

$$p \approx k - \frac{v_s}{v_F}|p_z|. \qquad (26)$$

Geometrically, the available phase space can be envisioned as pair of cones aligned along the p_z -axis, with the bases overlapping at $p_z = 0$, as depicted in Fig. 4. The radius attains is maximal value of k at $p_z = 0$ and tapers o as the magnitude of p_z increases. The vertices are reached at the following values of p_z:

$$|p_z|_{max} \approx \frac{v_F}{v_s}k. \qquad (27)$$

Finally, we determine the phonon wavevector q from the calculated value of p as a function of k. As shown in Eq. (22), the amplitudes of p_z and q_z will equal each other, since the electron and phonon dispersion centers lie on the same xy-plane. We label q_{xy} as the component of q perpendicular to the q_z -axis. For a given p_z and q_p pair, the amplitudes q_{xy}, k, and p form the 3 legs of a triangle for which q_p represents the angle between the sides of lengths k and p. Therefore, q_{xy} can be calculated as follows:

$$q_{xy} \approx \sqrt{k^2 + K^2 - 2kK\cos\theta_{\boldsymbol{k}}}, \qquad (28)$$

and since $q_z = - p_z$, the frequency !q of the emitted phonon is straightforwardly calculated from the speed of sound:

$$\omega_q = v_s\sqrt{q_{xy}^2 + q_z^2} \approx v_s\sqrt{p^2 + k^2 - 2pk\cos\theta_{\boldsymbol{p}} + p_z^2}. \quad (29)$$

Since $v_F >> v_s$ (by a factor of 400), the length of each cone is far longer than the diameter, implying that the approximation $q \approx |q_z| = |p_z| \approx p$ will be valid for nearly all of the available phase space.

B. Heat Transfer Rate: Having determined the phase space for the electron-phonon interaction, we are now in a position to calculate the heat transfer rate between the two modes from the composite interaction. Labeling the electron energy for a generic wavevector k' as $E_{k'}$, the matrix element corresponding to the electronic transition from k to p through the emission of a phonon in branch μ and wavevector q as $M^{\mu;q}{}_{k;p}$, the Bose-Einstein phonon occupation number for the mode frequency ω at temperature T as $n_T(\omega)$, and the Fermi-Dirac distribution value at T as f(T), the rate Q is determined through the following summation over initial carrier wavevectors k, final carrier wavevectors p, and phonon branches and wavevectors (μ; q) [31, 32]:

$$Q = \frac{2\pi}{\hbar}\sum_{\boldsymbol{k}}\sum_{\boldsymbol{p}}\sum_{\mu,\boldsymbol{q}}\left(E_{\boldsymbol{k}} - E_{\boldsymbol{p}}\right)\left|M_{\boldsymbol{k},\boldsymbol{p}}^{\mu,\boldsymbol{q}}\right|^2 \times \left(f(E_{\boldsymbol{k}}) - f(E_{\boldsymbol{p}})\right)\left(n_{T_L}(\omega_{\mu,\boldsymbol{q}}) - n_{T_e}(\omega_{\mu,\boldsymbol{q}})\right)\delta_{\boldsymbol{k},\boldsymbol{p}+\boldsymbol{q}} \times \delta\left(E_{\boldsymbol{k}} - E_{\boldsymbol{p}} - \hbar\omega_{\mu,\boldsymbol{q}}\right). \quad (30)$$

As previously discussed, the low temperature restricts the occupied phonon modes to the long-wavelength acoustic regime. The interaction between electrons and long-wavelength acoustic phonons is dominated by the deformation potential [33, 34], as recently applied to the interaction between bulk electrons and phonons in Cd_3As_2 [25, 35]. As discussed in our published paper, the equivalent matrix elements apply for the interaction between

surface electrons and bulk phonons. Therefore, the matrix element amplitude-squared reduces to a function varying solely with and linear in the phonon amplitude q:

$$\sum_{\mu} \left| M_{\boldsymbol{k},\boldsymbol{p}}^{\mu,\boldsymbol{q}} \right|^2 = \frac{C}{V} q, \tag{31}$$

where V represents the lattice volume and C is a constant that varies with the square of the deformation potential. Substituting this, along with the electron and phonon dispersion relationships into the expression for Q, we find that it takes the following form:

$$\begin{aligned} Q = \frac{2\pi}{\hbar} \sum_{\boldsymbol{k},\boldsymbol{p},\boldsymbol{q}} & \hbar v_F \Big(k - p_{xy} \Big) \frac{C}{V} q \Big(f(\hbar v_F k) - f(\hbar v_F p_{xy}) \Big) \\ & \times \Big(n_{T_L}(v_s q) - n_{T_e}(v_s q) \Big) \\ & \times \delta_{\boldsymbol{k},\boldsymbol{p}+\boldsymbol{q}} \delta \Big(\hbar v_F k - \hbar v_F p_{xy} - \hbar v_s q \Big). \end{aligned} \tag{32}$$

The summation is simplified in the limit $\Delta T << T$, where $T \approx T_e \approx T_L$ and ΔT is defined as $T_e - T_L$. We find that the Dirac and Kronecker delta functions combine to reduce the integral over the phase space volume to the double-cone phase space area derived previously, as expected. This yields the following expression for the carrier-phonon heat transfer rate due to intraband (valence-valence or conduction-conduction) transitions:

$$Q \approx \frac{AC}{2\pi^2 \hbar} \frac{v_s}{v_F} \left(\frac{\hbar v_s}{k_B T} \right) \frac{\Delta T}{T} \left(\frac{k_B T}{\hbar v_F} \right)^3 \left(\frac{k_B T}{\hbar v_s} \right)^4 \int_0^{\infty} dx x \int_0^{x} dy (x-y) y^3 \frac{e^y}{(e^y - 1)^2} \left(\frac{1}{e^x + 1} - \frac{1}{e^{x-y} + 1} \right). \tag{33}$$

Solving the integral numerically, we obtain a value of -32. Therefore, Q is further reduced to the following:

$$Q \approx -\frac{16ACk_B^6}{\pi^2\hbar^7 v_F^4 v_s^2} T^5 \Delta T. \qquad (34)$$

Next, we solve for the heat transfer rate due to interband transitions. We use the following expression:

$$Q_{inter} \approx \frac{AC}{2\pi^2\hbar}\frac{v_s}{v_F}\left(\frac{\hbar v_s}{k_B T}\right)\frac{\Delta T}{T}\left(\frac{k_B T}{\hbar v_F}\right)^3\left(\frac{k_B T}{\hbar v_s}\right)^4 \int_0^\infty dx x \int_x^\infty dy(y-x)y^3 \frac{e^y}{(e^y-1)^2}\left(\frac{1}{e^x+1}-\frac{1}{e^{x-y}+1}\right). \qquad (35)$$

Note that the constants in front of the integral are identical to that for the intraband case. Solving this integral numerically yields a value of -100. The total heat transfer rate Q_{total} from the surface carriers to the lattice vibrations is determined by multiplying the intraband rate Q by 2 (to account for both bands) and then summing with the interband rate Q_{inter}:

$$\begin{aligned} Q_{total} &= 2Q + Q_{inter} \\ &\approx -\frac{82ACk_B^6}{\pi^2\hbar^7 v_F^4 v_s^2} T^5 \Delta T. \end{aligned} \qquad (36)$$

In order to determine the heat transfer timescale, we substitute the previously derived relationship between the electron cooling rate and the rate of change of electron temperature from Eq. (10) into the left-hand-side of the above expression:

$$\begin{aligned} -\frac{10.8Ak_B^3}{\pi\hbar^2 v_F^2} T^2 \frac{d(\Delta T)}{dt} &\approx -\frac{82ACk_B^6}{\pi^2\hbar^7 v_F^4 v_s^2} T^5 \Delta T, \\ \frac{d(\Delta T)}{dt} &\approx -\frac{7.6Ck_B^3 T^3}{\pi\hbar^5 v_F^2 v_s^2} \Delta T. \end{aligned} \qquad (37)$$

As the result shows, the electron temperature decays exponentially toward the lattice temperature, with the rate varying as T^3.

The remaining task is to determine the value of the constant C, which derives from the electron-phonon matrix element. One method for doing so is by using the deformation potential of 20 eV measured by Jay-Gerin et al. [36]. This yields the following value for C, using a material density $\rho = 7 \times 10^3$ kg/m^3 [25]:

$$C = \frac{\hbar D^2}{4\rho v_s} = 1.7 \times 10^{-77}\ \mathrm{J^2 m^4}. \qquad (38)$$

This leads to the following heat transfer time constant:

$$\gamma \approx \frac{7.6 C k_B^3 T^3}{\pi \hbar^5 v_F^2 v_s^2} \approx \left(1.6 \times 10^6\ \mathrm{K^{-3} s^{-1}}\right) T^3. \qquad (39)$$

An alternative method for finding the deformation potential is by merging the experimental results from Weber et al. [37] with the theory provided by Lundgren and Fiete [25]. Specifically, Weber et al. used a bulk Cd_3As_2 sample intrinsically doped to a baseline electron density of 6×10^{23} m^{-3}, which corresponds to a Fermi energy of 170 meV and a Fermi temperature of 1130 K. Under these conditions, they observed a timescale of 3.1 ps for electron cooling by low-energy acoustic phonon emission at lattice temperatures of 80 K and 300 K. This scenario is addressed by Lundgren and Fiete's Equation (8), which models the heat transfer rate for $k_B T \ll E_f$ (where E_f is the Fermi energy):

$$\gamma = \frac{D^2 E_f^4}{3 k_B \hbar^4 v_F^5 \rho T}. \qquad (40)$$

We now substitute a temperature and rate data point from Weber et al. into this expression to calculate the deformation potential D. Since the limit $k_B T \ll E_f$ is much more valid for T = 80 K than for 300 K, we use the former as the temperature

corresponding to the rate $\gamma = (3.1\ \text{ps})^{-1}$ for the purposes of application to Eq. (40). This yields the following value for D:

$$D = \left(\frac{3k_B\hbar^4 v_F^5 \rho}{E_f^4} T\gamma\right)^{\frac{1}{2}} = 250\ \text{eV}. \qquad (41)$$

This leads to the following value for the coefficient C:

$$C = \frac{\hbar D^2}{4\rho v_s} = 2.7 \times 10^{-75}\ \text{J}^2\text{m}^4, \qquad (42)$$

which yields the following heat transfer time for our model:

$$\gamma \approx \frac{7.6Ck_B^3T^3}{\pi\hbar^5 v_F^2 v_s^2} \approx \left(2.5 \times 10^8\ \text{K}^{-3}\text{s}^{-1}\right)T^3. \qquad (43)$$

As will be discussed in the next section, the lower bound for the baseline temperature T (which will also set the minimum value for the heat transfer rate) will be about 0.35 K. For this temperature, the above two methods yield a lattice heating timescale approximately ranging from 93 ns to 15 μs.

It is worth comparing this timescale with the corresponding timescale for heat transfer between lattice phonons and bulk electrons (when the bulk is in the normal, non-superconducting phase). Based on Eq. (6) of Lundgren and Fiete [25], this timescale would be on the order of 7000 seconds, well over 8 orders of magnitude longer than even the upper bound value for the transfer time from surface electrons to the lattice phonons. This difference can be attributed to the vastly greater available phase space area for the surface electron interaction. Consequently, any heat transfer from the phonons to the bulk electrons is insignificant compared to that from the surface electrons to the phonons.

V. PHOTON-NUMBER RESOLVING DETECTION

We now describe the photon-number resolving detector scheme based on our theoretical findings. First, we address the question of whether the timescale for lattice temperature equilibration is much faster than the dissipation time through thermal conduction or radiative decay. Regarding the thermal conduction heat loss, we note that the contacts used for cooling the sample can be removed after the material reaches the refrigerator temperature. As a result, the heat dissipation time through thermal conduction will range on the order of several hours and can thus be ignored. Instead, we will focus on the radiative loss. Based on the results calculated for graphene, the electron-hole interband dipole moment for a 2D Dirac cone band structure is given as a function of photon radial frequency ω as follows [38]:

$$d_{c,v} = \frac{ev_F}{\omega}. \tag{44}$$

Substituting this into the well-known radiative decay rate expression based on the Einstein coefficients [39], we find that the radiative rate varies linearly with ω:

$$\begin{aligned} \Gamma_{rad}(\omega) &= \frac{\omega^3}{3\pi\epsilon_0\hbar c^3}\left|d_{c,v}(\omega)\right|^2 \\ &= \frac{e^2 v_F^2}{3\pi\epsilon_0\hbar c^3}\omega \\ &= \left(1.1\times 10^{-7}\right)\omega \end{aligned} \tag{45}$$

For frequencies up to 10 GHz, the radiative decay time is therefore 150 μs or greater. This is significantly longer than the electron-phonon heat transfer time calculated above, which is 15 μs or less, which in turn is much longer than the previously discussed electron-electron rethermalization time of tens of picoseconds [22]. Therefore, a rapid rethermalization of the electron population in the bands occurs before any radiative loss of the photoelectrons occurs.

Next, we address the question of heat transfer from the surface electronic modes directly to the bulk electronic modes. This would constitute a loss process, since it reduces the heat absorbed by

the bulk phonon modes. We note that the aforementioned spatial separation between bulk and surface electronic states renders this process unlikely. It is also worth comparing the heat capacity of the bulk electron modes to that of the phonon modes. To this end, in the temperature range 0.35-0.45 K (just over 0.5Tc), the superconducting state features approximately the same heat capacity as the normal state extrapolated to that temperature range. As such, we use the collective electron energy expression shown in Eq. (6), this time using the 3D rather than 2D Dirac cone dispersion to derive the density of states ρ(E):

$$\begin{aligned}\rho(E) &= \frac{dN}{dV_k}\frac{dV_k}{dk}\frac{dk}{dE} \\ &= \frac{V}{(2\pi)^3}\left(4\pi\left(\frac{E}{\hbar v_F}\right)^2\right)\frac{1}{\hbar v_F} \\ &= \frac{V}{2\pi^2\hbar^3 v_F^3}E^2,\end{aligned} \tag{46}$$

where V denotes the bulk volume. Substituting into Eq. (6), we find the following bulk thermal energy as a function of temperature:

$$\begin{aligned}U_{el,bulk}(T) &= \frac{V}{\pi^2\hbar^3 v_F^3}\int_0^\infty dE E^3 \frac{e^{-\frac{E}{k_B T}}+1}{\cosh\left(\frac{E}{k_B T}\right)+1} \\ &= \frac{V}{\pi^2\hbar^3 v_F^3}(k_B T)^4\frac{7\pi^4}{60} \\ &= \frac{7\pi^2 V k_B^4}{60\hbar^3 v_F^3}T^4.\end{aligned} \tag{47}$$

The bulk heat capacity is calculated by taking the derivative with respect to the temperature T:

$$C_{el,bulk}(T) = \frac{dU_{el,bulk}}{dT} = \frac{7\pi^2 V k_B^4}{15\hbar^3 v_F^3}T^3. \tag{48}$$

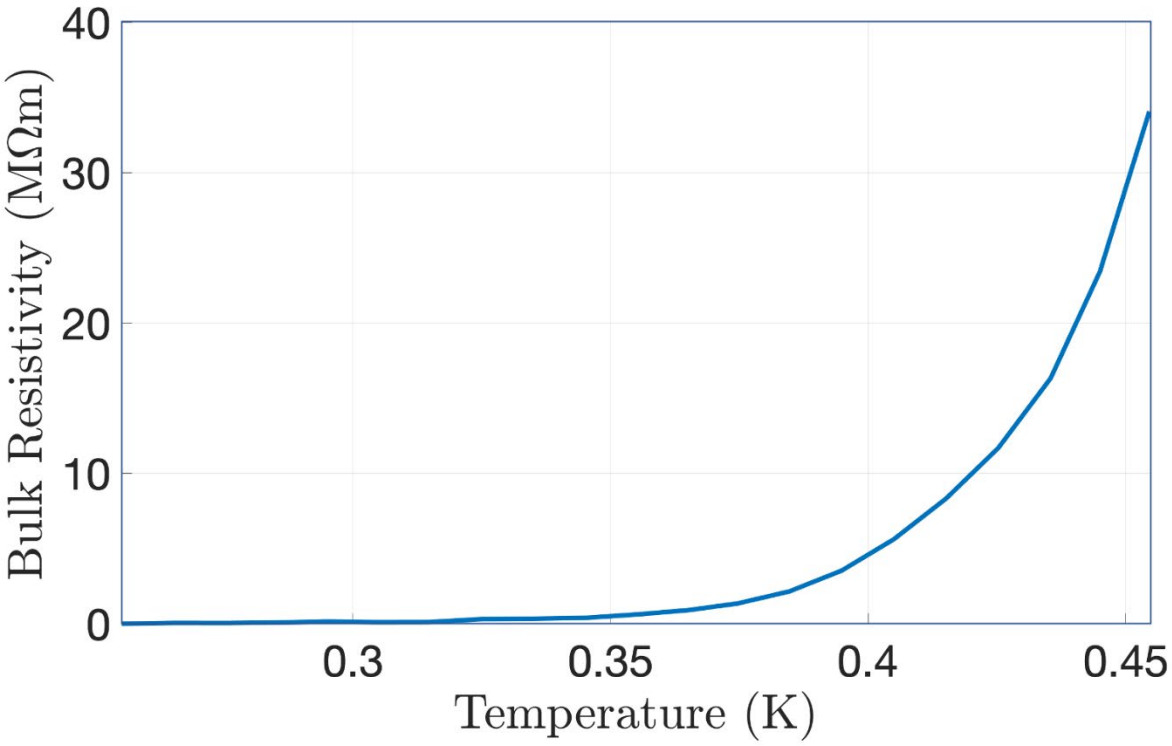

Figure 5: Resistivity (in megaohm-meters) versus temperature (in kelvins) for bulk Cd_3As_2.

Comparing this to the phonon heat capacity (see Eq. (19)), we find that the phonon heat capacity is greater by a factor of approximately (vF/vs)3, i.e. more than 7 orders of magnitude. This massive disparity can be explained by the fact that near the Fermi level, the electron group velocity vastly exceeds the phonon group velocity, resulting in a far greater density of states for the phonon modes than for the electron modes. We thus conclude that the energy of the absorbed photons is safely transferred to, first, the rethermalization of the carrier band populations, and then, to the bulk phonon modes to elevate the bulk temperature. We now discuss how the bulk temperature is measured. Since the elevated bulk temperature will increase the bulk resistance of the superconducting bulk states as shown in Fig. 5, we measure the zero-bias resistivity across the bulk (using a lock-in amplifier) as a proxy for the temperature. This is advantageous relative to infrared-based bolometry since it does not perturb the electronic structure of the bulk, as well as due to the fact that electrical signals can be measured in ultrafast picosecond-range intervals [40]. We manufactured a Cd_3As_2 device to measure the superconducting bulk resistivity as a function of sample temperature. To this end, it is important to note the lower bounds for the dimensions of each Cd_3As_2 crystal. The goal of the device is to measure photons in the transmon

frequency range, i.e. 5 - 7 GHz [41, 42]. For a Dirac cone dispersion with Fermi velocity vF , a photon of frequency f is resonant with the band gap at the following band wavevector:

$$k = \frac{\pi f}{v_F}. \qquad (49)$$

Therefore, in order for resonance to exist at photon frequencies as low as 5 GHz, the maximum length of each Bloch state in reciprocal space must be $\Delta k \approx 1.6 \times 10^4$ m^{-1}, thus implying that the minimum length of the Cd3As2 surface along each dimension is $2\pi/\Delta k = 0.4$ mm. We also assume that the depth of the lattice is limited by design constraints to a minimum value of 20 nm, since this is the minimum thickness that has been achieved with an MBE technique [14]. For a photon frequency of 5 GHz and crystal dimensions of 0.4mm by 0.4 mm by 20 nm, the single-photon temperature gain is calculated by substituting the values N = 1, $\omega = \pi \times 10^{10}$ s^{-1}, and V = 3.2×10^{-15} m^3 into Eq. (21) and linearizing:

$$\begin{aligned} \Delta T &= \frac{1}{4T^3}\left(4.13 \times 10^{-35}\ \mathrm{m^3K^4s}\right)\frac{N\omega}{V} \\ &= \frac{1.0 \times 10^{-10}\ \mathrm{K^4}}{T^3}. \end{aligned} \qquad (50)$$

For temperatures above our minimum refrigerator temperature of 0.25 K, the temperature gain due to the absorption of a single photon is below 6.5 nK, which confirms our previous assumption that $\Delta T << T$.

Finally, we use the single-photon temperature gain to determine the corresponding increase in bulk resistance. Figure 5 depicts the experimental values for zero-bias resistivity as a function of temperature in bulk Cd_3As_2 in the superconducting regime. For temperatures above 0.35 K, the resistivity steadily increases with temperature. We will therefore use 0.35 K to 0.45 K as the range of baseline temperatures for which we will determine the single-photon bulk resistance

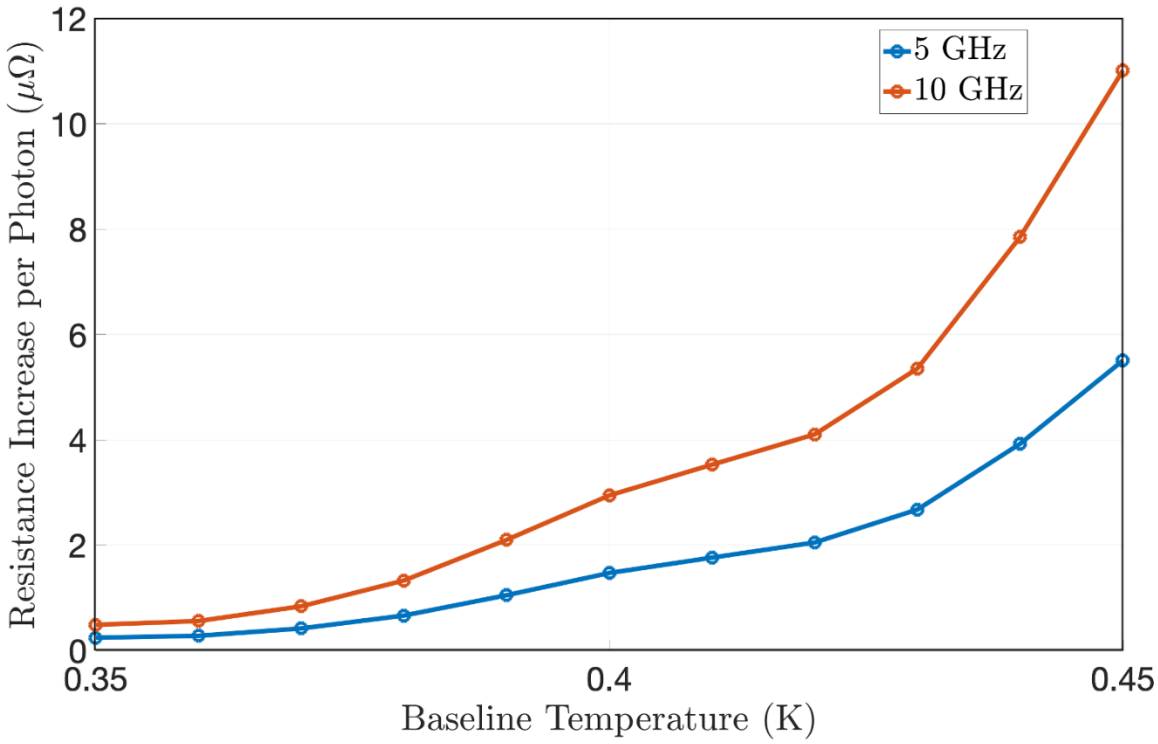

Figure 6: Plots of bulk resistance gain (in microohms) due to absorption of a single photon versus baseline temperature for photon frequencies f = 5; 10 GHz given sample dimensions 0.4 mm by 0.4 mm by 20 nm.

gain. For a square lattice surface, the bulk resistance scales linearly with resistivity as 1/d, where d denotes the lattice depth. Therefore, the single-photon resistance gain relates to the slope of the resistivity with respect to temperature (dρ/dT) and the single-photon temperature gain (ΔT) as follows:

$$\Delta R = \frac{1}{d}\frac{d\rho}{dT}\Delta T \qquad (51)$$

For the aforementioned sample dimensions, d = 20 nm. Substituting the expression for ΔT from Eq. (50), we find that the single-photon resistance gain ΔR solely becomes a function of the baseline temperature T:

$$\Delta R = \frac{5.0 \times 10^{-3}\ \mathrm{m^{-1}K^4}}{T^3} \frac{d\rho}{dT} \qquad (52)$$

Figure 6 depicts the resistance gain due to the absorption of a single photon for baseline temperatures ranging from 0.35 K to 0.45 K for the selected photon frequencies of 5 GHz and 10 GHz. For temperatures of 0.39 K and above, the single-photon resistance gain will be greater than 1 μΩ for photon frequencies as low as 5 GHz, an increase which is certainly measurable using a commercially available micro-ohm meter (such as the Keysight 34420A NanoVolt/Micro-Ohm Meter by Keysight Technologies) or with a Corbino geometry sample which can even measure sub-micro-ohm resistance [43]. This property can therefore be exploited in order to precisely determine the number of absorbed photons for a known frequency.

It is worth discussing the effect of impurities on the properties of the detector. Normally, the presence of charged impurities would lead to a shift of the Fermi level away from the Dirac point, which in turn would degrade the performance of the detector by hindering photon absorption in the microwave frequency range. However, recent experiments have demonstrated that Cd_3As_2 is easily doped, either chemically [44] or electrostatically [45]. Therefore, the Fermi level of the surface state can be tuned so as to coincide with the Dirac point, as desired. Since the electronic structure of the surface is decoupled from that of the bulk, it is feasible to specifically dope the former while leaving the latter unaltered.

Finally, we address the issue of dark count. Due to the cryogenic (sub-Kelvin) refrigerator temperature, the dark count should be negligible, as previously demonstrated for transition-edge sensors under similar temperature conditions [46]. Nonetheless, precise experimental determination of the dark count for the Cd_3As_2 detector would serve as an important topic for future research.

VI. DISCUSSIONS AND CONCLUSION

We demonstrated a microwave photon-number resolving detector based on the topological surface states of Cd_3As_2 material. The number of photons absorbed is produced after measuring the increased resistivity of the superconducting bulk. For this, we derived in detail how much bulk temperature would elevate as a function of the absorbed number of photons and the photon frequency. We showed that the energy of the absorbed photon is rapidly transferred first to the rethermalized distribution of the surface state electron band population. Then, the electron band energy is quickly transferred to the bulk phonon modes through the deformation potential coupling. The bulk temperature is thus elevated, and finally, the superconducting bulk increases resistance, which is measured to resolve the absorbed number of photons. To address how quickly the energy is transferred from the surface electron to the bulk phonon modes, we derived the deformation potential electron-phonon coupling rate by calculating the transition matrix element and the phase space volume. As a result, we concluded that the coupling time constant ranged from nanoseconds to microseconds. Therefore, it is expected that the number of absorbed photons would be measured within several milliseconds after the absorption happens.

Our proposed scheme accomplishes rapid photon detection based on quick (or even continuous) and accurate bulk resistance measurement. Direct measurement of the elevated temperature in bulk does not provide a feasible path due to the slow detection speed and the measurement noise in the extremely small differential temperature. It is essential to understand why the use of Cd_3As_2 bulk's semimetal feature for absorbing microwave photons is avoided. Recall that, if the baseline temperature is set above the critical temperature, the bulk's electronic bands do not open a gap, which allows the bulk electrons to be excited by the microwave photons. However, detecting the excited electron is extremely difficult for two main reasons. First, the bulk photoelectron may easily join the resistance-measuring current and be lost in the measurement process. Second, the photoelectron's energy transfer to the bulk temperature is extremely inefficient due to the reduced phase space of 3D electrons, risking the loss of photoelectrons via radiative decay rather than energy transfer to the bulk phonon modes. In contrast, the photon absorption from the surface state electrons almost surely transfers the energy to the bulk phonon modes.

Equally important is understanding the difference between our proposed scheme and an alternative device structure of a Dirac 2D material such as graphene on the surface of a bulk superconductor. A pure graphene layer indeed does not possess a superconductor state [47], and thus can be used as a Dirac cone photon absorber of microwave photons even at a very low temperature. However, it is more difficult to fabricate this device than Cd_3As_2 which simultaneously has both bulk superconductor and surface states. In addition, the hybrid structure suffers from inefficient electronic energy transfer to the bulk phonons due to the mismatch of lattice constants. Instead, as previous research on graphene single-photon detectors has shown, the inefficient electronic energy transfer to phonons is used for efficient capture of the photoelectron in the electrodes [48]. However, in this case, the photon-number resolving feature is lost. In comparison, our scheme utilizes the surface state electrons of Cd_3As_2 as a microwave photon absorber and the bulk superconductor of the same material for detecting the number of photons absorbed. The distinct advantage of our method is to provide a deterministic photon-number resolving capability in microwave photon detection. It is also worth understanding the advantage that our scheme offers over traditional transition-edge-sensor (TES) based detectors. Due to the need for a significant voltage bias in measuring the resistance of the TES bulk, a large source-drain current is generated, causing undesired side effects such as flicker noise. A Cd_3As_2-based detector avoids this issue by enabling zero-bias resistance measurement.

We now discuss the design strategy of maximizing the photon absorption probability of the device. Note that each crystal surface features an absorption rate of 0.3-0.6%. Therefore, it is possible to have a near unity quantum efficiency if about 2000 bulk crystal layers are vertically stacked in a heterostructure (such that they are in series from the point of view of the incoming photon), while measuring the bulk zero-bias resistivity for each of the crystals separately. With the advent of more advanced manufacturing techniques, such heterostructure is increasingly becoming possible [50]. Another means of achieving the same goal is by placing a single-layer detector in an optical cavity bounded by high-reflectivity mirrors. Since Bragg mirrors can feature transmittance rates as low as 1 ppm [51], the total probability that a photon is lost through one of the mirrors will be negligible even after thousands of round trips through the cavity, thus ensuring a near-unity detector efficiency.

REFERENCES

[1] A. Divochiy, F. Marsili, D. Bitauld, A. Gaggero, R. Leoni, F. Mattioli, A. Korneev, V. Seleznev, N. Kaurova, O. Minaeva, G. Gol'tsman, K. G. Lagoudakis, M. Benkhaoul, F. Levy, and A. Fiore, Superconducting nanowire photon-number-resolving detector at telecommunication wavelengths, Nat. Photon. 2, 302 (2008).

[2] B. E. Kardyna l, Z. L. Yuan, and A. J. Shields, An avalanche-photodiode-based photon-number-resolving detector, Nat. Photon. 2, 425 (2008).

[3] D. Rosenberg, A. E. Lita, A. J. Miller, and S. W. Nam, Noise-free high-efficiency photon-number-resolving detectors, Phys. Rev. A 71, 061803(R) (2005).

[4] F.-G. Deng, X.-H. Li, H.-Y. Zhou, and Z.-j. Zhang, Improving the security of multiparty quantum secret sharing against Trojan horse attack, Phys. Rev. A 72, 044302 (2005).

[5] X.-B. Chen, X.-X. Niu, X.-J. Zhou, and Y.-X. Yang, Multi-party quantum secret sharing with the single particle quantum state to encode the information, Quant. Inf. Proc. 12, 365 (2013).

[6] I. Afek, O. Ambar, and Y. Silberberg, High-NOON States by Mixing Quantum and Classical Light, Science 328, 879 (2010).

[7] A. A. Houck, J. A. Schreier, B. R. Johnson, J. M. Chow, Jens Koch, J. M. Gambetta, D. I. Schuster, L. Frunzio, M. H. Devoret, S. M. Girvin, and R. J. Schoelkopf, Controlling the Spontaneous Emission of a Superconducting Transmon Qubit, Phys. Rev. Lett. 101, 080502 (2008).

[8] G. Romero, J. J. Garcia-Ripoll, and E. Solano, Microwave Photon Detector in Circuit QED, Phys. Rev. Lett. 102, 173602 (2009).

[9] K. Inomata, Z. Lin, K. Koshino, W. D. Oliver, J.-S. Tsai, T. Yamamoto, and Y. Nakamura, Single microwavephoton detector using an artificial type three-level system, Nat. Commun. 7, 12303 (2016).

[10] A. Poudel, R. McDermott, and M. G. Vavilov, Quantum efficiency of a microwave photon detector based on a current-biased Josephson junction, Phys. Rev. B 86, 174506 (2012).

[11] B. Royer, A. L. Grimsmo, A. Choquette-Poitevin, and A. Blais, Itinerant Microwave Photon Detector, Phys. Rev. Lett. 120, 203602 (2018).

[12] T. Liang, Q. Gibson, M. N. Ali, M. Liu, R. J. Cava, and N. P. Ong, Ultrahigh mobility and giant magnetoresistance in the Dirac semimetal Cd_3As_2, Nat. Mater. 14, 280 (2015).

[13] M. N. Ali, Q. Gibson, S. Jeon, B. B. Zhou, A. Yazdani, and R. J. Cava, The Crystal and Electronic Structures of Cd_3As_2, the Three-Dimensional Electronic Analogue of Graphene, Inorg. Chem. 53, 4062 (2014).

[14] T. Schumann, L. Galletti, D. A. Kealhofer, H. Kim, M. Goyal, and S. Stemmer, Observation of the Quantum Hall Effect in Confined Films of the Three-Dimensional Dirac Semimetal Cd_3As_2, Phys. Rev. Lett 120, 016801 (2018).

[15] M. Uchida, Y. Nakazawa, S. Nishihaya, K. Akiba, M. Kriener, Y. Kozuka, A. Miyake, Y. Taguchi, M. Tokunaga, N. Nagaosa, Y. Tokura, and M. Kawasaki, Quantum Hall states observed in thin films of Dirac semimetal Cd_3As_2, Nat. Commun. 8, 2274 (2017).

[16] H. Yi, Z. Wang, C. Chen, Y. Shi, Y. Feng, A. Liang, Z. Xie, S. He, J. He, Y. Peng, X. Liu, Y. Liu, L. Zhao, G. Liu, X. Dong, J. Zhang, M. Nakatake, M. Arita, K. Shimada, H. Namatame, M. Taniguchi, Z. Xu, C. Chen, X. Dai, Z. Fang, and X. J. Zhou, Evidence of Topological Surface State in Three-Dimensional Dirac Semimetal Cd_3As_2, Sci. Rep. 4, 6106 (2015).

[17] M. Goyal, H. Kim, T. Schumann, L. Galletti, A. A. Burkov, and S. Stemmer, Surface states of strained thin films of the Dirac semimetal Cd_3As_2, Phys. Rev. Mater. 3, 064204 (2019).

[18] M. Neupane, S.-Y. Xu, R. Sankar, N. Alidoust, G. Bian, C. Liu, I. Belopolski, T.-R. Chang, H.-T. Jeng, H. Lin, A. Bansil, F. Chou, and M. Z. Hasan, Observation of a three-dimensional topological Dirac semimetal phase in high-mobility Cd_3As_2, Nat Commun. 5, 3786 (2014).

[19] W. Yu, R. Haenel, M. A. Rodriguez, S. R. Lee, F. Zhang, M. Franz, D. I. Pikulin, and W. Pan, Zero-bias conductance peak in Dirac semimetal-superconductor devices, Phys. Rev. Research 2, 032002(R) (2020).

[20] J. Bardeen, L. N. Cooper, and J. R. Schrieffer, Theory of Superconductivity, Phys. Rev. 108, 1175 (1957).

[21] D. Soh, 2D materials and nonlinear quantum optics (Stanford University, Stanford, California, 2019).

[22] M. T. Mihnev, F. Kadi, C. J. Divin, T. Winzer, S. Lee, C.-H. Liu, Z. Zhong, C. Berger, W. A. de Heer, E. Malic, A. Knorr, and T. B. Norris, Microscopic origins of the terahertz carrier relaxation and cooling dynamics in graphene, Nat. Commun. 7, 11617 (2016).

[23] D. Sun, Z.-K. Wu, C. Divin, X. Li, C. Berger, W. A. de Heer, P. N. First, and T. B. Norris, Ultrafast Relaxation of Excited Dirac Fermions in Epitaxial Graphene Using Optical Differential Transmission Spectroscopy, Phys. Rev. Lett. 101, 157402 (2008).

[24] J. M. Dawlatya, S. Shivaraman, M. Chandrashekhar, F. Rana, and M. G. Spencer, Measurement of ultrafast carrier dynamics in epitaxial graphene, Appl. Phys. Lett. 92, 042116 (2008).

[25] R. Lundgren and G. A. Fiete, Electronic cooling in Weyl and Dirac semimetals, Phys. Rev. B 92, 125139 (2015).

[26] P. Debye, Zur Theorie der spezischen Wärmen, Annalen der Physik 344, 789 (1912).

[27] C. Kittel, Introduction to Solid State Physics (John Wiley & Sons, Inc., Hoboken, NJ, 2005).

[28] "Debye Model For Specific Heat." Engineering, 18 May, 2020, Libretexts. eng.libretexts.org/Bookshelves/Materials Science/Supplemental Modules (Materials Science)/Electronic Properties/Debye Model For Specific Heat. Accessed 25 June, 2020.

[29] Z. Wang, H. Weng, Q. Wu, X. Dai, and Z. Fang, Three dimensional Dirac semimetal and quantum transport in Cd_3As_2, Phys. Rev. B 88, 125427 (2013).

[30] S. S. Kubakaddi and T. Biswas, Hot electron cooling in Dirac semimetal Cd_3As_2 due to polar optical phonons, J. Phys.: Condens. Matter 30, 265303 (2018).

[31] J. K. Viljas and T. T. Heikkila, Electron-phonon heat transfer in monolayer and bilayer graphene, Phys. Rev. B 81, 245404 (2010).

[32] F. C. Wellstood, C. Urbina, and J. Clarke, Hot-electron effects in metals, Phys. Rev. B 49, 5942 (1994).

[33] J. Bardeen and W. Shockley, Deformation Potentials and Mobilities in Non-Polar Crystals, Phys. Rev. 80, 72 (1950).

[34] C. Herring and E. Vogt, Transport and Deformation-Potential Theory for Many-Valley Semiconductors with Anisotropic Scattering, Phys. Rev. 101, 944 (1956).

[35] K. S. Bhargavi and S. S. Kubakaddi, Electron cooling in three-dimensional Dirac fermion systems at low temperature: Effect of screening, Phys. Status Solidi RRL 10, 248 (2016).

[36] J.-P. Jay-Gerin, M. J. Aubin, and L.-G. Caron, Thermoelectric power and transverse Nernst-Ettingshausen coefficient of Cd_3As_2 at 300 K, Phys. Rev. B 18, 4542 (1978).

[37] C. P. Weber, E. Arushanov, B. S. Berggren, T. Hosseini, N. Kouklin, and A. Nateprov, Transient reflectance of photoexcited Cd_3As_2, Appl. Phys. Lett. 106, 231904 (2015).

[38] X. Yao and A. Belyanin, Nonlinear optics of graphene in a strong magnetic field, J. Phys.: Condens. Matter 25, 054203 (2013).

[39] R. C. Hilborn, Einstein coefficients, cross sections, f values, dipole moments, and all that, Am. J. Phys. 50, 982 (1982).

[40] Y. Yang, R. B. Wilson, J. Gorchon, C.-H. Lambert, S. Salahuddin, and J. Bokor, Ultrafast magnetization reversal by picosecond electrical pulses, Sci. Adv. 3, e1603117 (2017).

[41] Y. Reshitnyk, M. Jerger, and A. Fedorov, 3D microwave cavity with magnetic flux control and enhanced quality factor, EPJ Quant. Technol. 3, 13 (2016).

[42] S. Miller, A tunable 20 GHz transmon qubit in a 3D cavity (unpublished master's thesis, Quantum Device Lab Laboratory for Solid State Physics, Swiss Federal Institute of Technology, Zurich, 2018).

[43] D. C. Tsui, H. L. Stormer, and A. C. Gossard, Zero resistance state of two-dimensional electrons in a quantizing magnetic field, Phys. Rev. B 25, 1405(R) (1982).

[44] Z. K. Liu, J. Jiang, B. Zhou, Z. J.Wang, Y. Zhang, H. M. Weng, D. Prabhakaran, S-K. Mo, H. Peng, P. Dudin, T. Kim, M. Hoesch, Z. Fang, X. Dai, Z. X. Shen, D. L. Feng, Z. Hussain, and Y. L. Chen, A stable three-dimensional topological Dirac semimetal Cd_3As_2, Nat. Mater. 13, 677 (2014).

[45] Y. Liu, C. Zhang, X. Yuan, T. Lei, C.Wang, D. Di Sante, A. Narayan, L. He, S. Picozzi, S. Sanvito, R. Che, and F. Xiu, Gate-tunable quantum oscillations in ambipolar Cd_3As_2 thin films, NPG Asia Mater. 7, e221 (2015).

[46] K. Niwa, T. Numata, K. Hattori, and D. Fukuda, Fewphoton color imaging using energy-dispersive superconducting transition-edge sensor spectrometry, Sci. Rep. 7, 45660 (2017).

[47] N. B. Kopnin and E. B. Sonin, BCS Superconductivity of Dirac Electrons in Graphene Layers, Phys. Rev. Lett. 100, 246808 (2008).

[48] E. D. Walsh, D. K. Efetov, G.-H. Lee, M. Heuck, J. Crossno, T. A. Ohki, P. Kim, D. Englund, and K.C. Fong, Graphene-Based Josephson-Junction Single-Photon Detector, Phys. Rev. Appl. 8, 024022 (2017).

[49] T. Gerrits, B. Calkins, N. Tomlin, A. E. Lita, A. Migdall, R. Mirin, and S. W. Nam, Extending single-photon optimized superconducting transition edge sensors beyond the single-photon counting regime, Opt. Express 20, 23798 (2012).

[50] S. Tongay, W. Fan, J. Kang, J. Park, U. Koldemir, J. Suh, D. S. Narang, K. Liu, J. Ji, J. Li, R. Sinclair, and J. Wu, Tuning Interlayer Coupling in Large-Area Heterostructures with CVD-Grown MoS_2 and WS_2 Mon- layers, Nano Lett. 14, 3185 (2014).

[51] R. Paschotta, article on 'supermirrors' in the RP Photonics Encyclopedia, accessed on 2020-11-25.

APPENDIX A. PROJECT OUTPUTS -- PUBLICATIONS

Published

- Evidence of decoupling of surface and bulk states in Dirac semimetal Cd_3As_2, Nanotechnology 33, 415002 (2022). DOI: 10.1088/1361-6528/ac7c25
- Magneto-transport evidence for strong topological insulator phase in $ZrTe_5$, Nature Communications 12, 6758 (2021). DOI: 10.1038/s41467-021-27119-5 (partially funded by SAA plus-up)
- Normal vector approach to Fourier modal scattering from planar periodic photonic structures, Photonics and Nanostructures - Fundamentals and Applications 43, 100864 (2021). DOI:10.1016/j.photonics.2020.1008641125
- Structure-property and thermodynamic relationships in rare earth (Y, Eu, Pr) iridate pyrochlores, Journal of Solid State Chemistry 299, 122163 (2021). DOI:10.1016/j.jssc.2021.122163
- Microwave response in a topological superconducting quantum interference device, Scientific Reports 11, 8615 (2021). DOI:10.1038/s41598-021-88035-8
- Microwave Photon Number Resolving Detector Using the Topological Surface State of Superconducting Cadmium Arsenide, Phys. Rev. Research 3, 023046 (2021). DOI:10.1103/PhysRevResearch.3.023046
- Unraveling the Topological Phase of $ZrTe_5$ via Magnetoinfrared Spectroscopy, Phys. Rev. Lett. 125, 046403 (2020). DOI: 10.1103/PhysRevLett.125.046403 (partially funded by SAA plus-up)
- Single-Crystal Synthesis and Characterization of Copper-Intercalated $ZrTe_5$, Crystal Growth & Design 20, 699 (2020), DOI: 10.1021/acs.cgd.9b01125. *Cover Art Published.*
- Electronic transport properties of a lithium-decorated $ZrTe_5$ thin film, Scientific Reports 10, 3537 (2020), DOI: 10.1038/s41598-020-60545-x

Under review

- Leggett Modes in Dirac Semimetals, arXiv:2205.15995, submitted to Nature Physics
- Ultra-High-Precision Detection of Single Microwave Photons based on a Hybrid System between Majorana Zero Mode and a Quantum Dot, arXiv:2206.06521, submitted to Phys. Rev. Research
- Effective g-factor and phase-coherent transport in InAsSb/InSb double quantum wells", submitted to Phys. Rev. Materials (partially funded by SAA plus-up).

DISTRIBUTION

Email—Internal

Name	Org.	Sandia Email Address
Tina M. Nenoff	01800	tmnenof@sandia.gov
David Rademacher	01874	dradema@sandia.gov
Paul Davids	05265	pdavids@sandia.gov
Wei Pan	08342	wpan@sandia.gov
Eric Chatterjee	08648	echatte@sandia.gov
Daniel Soh	08648	dbsoh@sandia.gov
Ashfia Huq	08342	ahuq@sandia.gov
Christian Mailhiot	08340	cmailhi@sandia.gov
Technical Library	01177	libref@sandia.gov

This page left blank

Sandia National Laboratories

Sandia National Laboratories is a multimission laboratory managed and operated by National Technology & Engineering Solutions of Sandia LLC, a wholly owned subsidiary of Honeywell International Inc. for the U.S. Department of Energy's National Nuclear Security Administration under contract DE-NA0003525.